Solar nebula magnetic fields recorded in the Semarkona meteorite

Roger R. Fu[1]*, Benjamin P. Weiss[1], Eduardo A. Lima[1], Richard J. Harrison[2], Xue-Ning Bai[3,4], Steven J. Desch[5], Denton S. Ebel[6], Clement Suavet[1], Huapei Wang[1], David Glenn[3], David Le Sage[7], Takeshi Kasama[8], Ronald L. Walsworth[3,7], Aaron T. Kuan[9]

[1]Department of Earth, Atmospheric and Planetary Sciences, Massachusetts Institute of Technology (MIT), Cambridge, MA, USA

[2]Department of Earth Sciences, University of Cambridge, Cambridge, UK

[3]Harvard-Smithsonian Center for Astrophysics, Cambridge, MA, USA

[4]Hubble Fellow

[5]School of Earth and Space Exploration, Arizona State University, Tempe, AZ, USA

[6]Department of Earth and Planetary Sciences, American Museum of Natural History (AMNH), New York, NY, USA

[7]Department of Physics, Harvard University, Cambridge, MA, USA

[8]Center for Electron Nanoscopy, Technical University of Denmark, Kongens Lyngby, Denmark

[9]School of Engineering and Applied Science, Harvard University, Cambridge, MA, USA

*To whom correspondence should be addressed. Email: rogerfu@mit.edu

Magnetic fields are proposed to have played a critical role in some of the most enigmatic processes of planetary formation by mediating the rapid accretion of disk material onto the central star and the formation of the first solids. However, there have been no direct experimental constraints on these fields. Here we show that dusty olivine-bearing chondrules from the Semarkona meteorite were magnetized in a nebular field of 54±21 μT. This intensity supports chondrule formation by nebular shocks or planetesimal collisions rather than by electric currents, the x-wind, or other mechanisms near the sun. This implies that background magnetic fields in the terrestrial planet-forming region were likely 5-54 μT, which is sufficient to account for the bulk of mass and angular momentum transport in protoplanetary disks.

Astronomical observations of young stellar objects indicate that early planetary systems evolve through a protoplanetary disk phase in <5 million years (My) following the collapse of their parent molecular clouds (*1, 2*). Disk evolution on such short timescales requires highly efficient inward transport of mass accompanied by outward angular momentum transfer, which allows disk material to accrete onto the central star while delivering angular momentum out of the protoplanetary system.

The mechanism of this rapid mass and angular momentum redistribution remains unknown. Several proposed processes invoke a central role for nebular magnetic fields. Among these, the magnetorotational instability (MRI) and magnetic braking predict magnetic fields with intensities of ~100 μT at 1 AU in the active layers of the disk (*3, 4*). Alternatively, transport by magnetocentrifugal wind (MCW) requires large-scale, ordered magnetic fields stronger than ~10 μT at 1 AU. Finally, non-magnetic effects such as the baroclinic and Goldreich-Schubert-Fricke instabilities may be the dominant mechanism of angular momentum transport in the absence of sufficiently strong magnetic fields (*5*). Direct measurement of magnetic fields in the planet-forming regions of the disk can potentially distinguish among and constrain these hypothesized mechanisms.

Although current astronomical observations cannot directly measure magnetic fields in planet-forming regions [(*6*); supplementary text], paleomagnetic experiments on meteoritic materials can potentially constrain the strength of nebular magnetic fields. Chondrules are millimeter-sized lithic constituents of primitive meteorites that formed in transient heating events in the solar nebula. If a stable field was present during cooling, they should have acquired a thermoremanent magnetization (TRM), which can be characterized via paleomagnetic experiments. Besides assessing the role of magnetic fields in disk evolution, such paleomagnetic measurements would constrain the currently unknown mechanism of chondrule formation.

Chondrules likely constituted a significant fraction of the mass of asteroids and terrestrial planet precursors and may have facilitated the accretion of the first planetesimals (*7, 8*). The formation of chondrules therefore very likely represents a key stage in the evolution of the early solar system. The ambient magnetic field strength is a distinguishing characteristic among chondrule formation models. The x-wind model implies strong stellar fields of >80-400 μT (*9*). In contrast, magnetic fields in the nebular shock and planetesimal collision models are likely significantly lower than 100 μT (*10, 11*).

Previous paleomagnetic measurements of individual chondrules have focused mostly on the Allende CV chondrite (*12*). However, due to extensive aqueous alteration on the CV parent body, magnetic phases in Allende chondrules are secondary and do not retain pre-accretional magnetization [i.e., magnetization acquired after the last heating of chondrules in the nebula and before the accretion of the meteorite's parent body; (*13*)]. Reliable recovery of pre-accretional magnetization requires samples that have avoided significant post-accretional remagnetization processes.

Among the most pristine known meteorites is the Semarkona LL3.00 ordinary chondrite. We conducted paleomagnetic studies on Semarkona, focusing in particular on dusty olivine-bearing chondrules (Fig. 1). Dusty olivine crystals consist of sub-micrometer sized grains of nearly pure body centered cubic (bcc) Fe (kamacite) embedded in forsteritic olivine (*14*). Such olivine grains are found in approximately one in ten chondrules in ordinary chondrites.

Due to their unique compositional and magnetic properties, dusty olivine grains are expected to retain pre-accretional magnetization. The small grain size of dusty olivine metal implies that most are in the single domain (SD) or single vortex (SV) states, which can retain stable magnetization over the history of the solar system (*15-18*). Further, the Ni-poor composition (Ni <2 wt%) of dusty olivine metal precludes metamorphic recrystallization (*14, 19*). The domain states of dusty olivine metals imply very high coercivities ranging up to >200 mT, as confirmed by our demagnetization experiments (see below). The magnetization of grains with such high coercivities should not have been significantly altered by the low shock pressures likely experienced by Semarkona [4-10 GPa (*20, 21*)]. Finally, the low porosities of the surrounding olivine crystals have protected metal from aqueous alteration (Fig. 1B).

The distinctive, high coercivities of dusty olivine grains allow for the isolation of their remanent magnetization during alternating field (AF) demagnetization as larger (10-100 μm) mesostasis metal grains are expected to demagnetize at AF levels <50 mT (*22*). Furthermore, since the post-accretional peak metamorphic temperature of Semarkona was likely only 200-260˚C (*23, 24*), pre-accretional remanence in dusty olivine metals should be isolated upon laboratory (1 hour duration) thermal demagnetization to <450˚C assuming that metamorphism lasted ~5 My (*15, 18*). In summary, no known post-accretional process is likely to have compromised pre-accretional remanent magnetization in Semarkona dusty olivines; strong field AF demagnetization or thermal demagnetization above ~450˚C is expected to isolate the pre-accretional component of magnetization.

We isolated eight dusty olivine-bearing chondrules from two 15 mm × 10 mm × 150 μm thick sections of Semarkona provided by the American Museum of Natural History (AMNH). Both sections contain fusion crust along one edge. We also extracted five non-dusty olivine-bearing chondrules and twenty-nine bulk (i.e., mixed matrix and chondrule) samples to characterize any post-accretional overprints. All extracted samples are mutually oriented to within 5˚. Due to their weak moments [natural remanent magnetization (NRM) ranging between 10^{-10} and 3×10^{-12} Am^2 prior to demagnetization], chondrules were measured using the Superconducting Quantum Interference Device (SQUID) Microscope (*25, 26*) at the MIT Paleomagnetism Laboratory (Fig. 2). Supporting magnetic imaging measurements with higher spatial resolution were performed using a nitrogen-vacancy (NV) quantum diamond microscope (supplementary text).

Bulk samples were subjected to AF demagnetization up to 85-145 mT or thermal demagnetization up to 580˚C. We identified three unidirectional post-accretional overprints in our Semarkona samples: two low coercivity (LCa and LCb) and one medium coercivity (MCa) components. Twenty bulk samples carry the LCa overprint blocked up to between 4.5 and 13 mT (Fig. 3). This component is present in both fusion crust material and meteorite interior samples, indicating that it was acquired after arrival on Earth. Removal of the LCa magnetization during thermal demagnetization to only 70˚C indicates that it is likely a viscous remanent magnetization (VRM) acquired during long-term exposure to the Earth's field.

In contrast, the MCa overprint is only present in samples within 4.7 mm of the fusion crust. The mean paleointensity of this component based on the isothermal remanent magnetization (IRM) and anhysteretic remanent magnetization (ARM) normalization methods (76 μT) is within uncertainty of the Earth's magnetic field. We conclude that MCa component was acquired during heating from atmospheric passage. Finally, a small subset of seven samples from one edge of our Semarkona section carry the LCb overprint, which is completely removed by AF demagnetization up to 10.5 to 30 mT. The high intensity of the LCb component (NRM to saturation IRM ratio of 0.23) suggests that it was acquired during exposure to artificial magnetic fields. Only two dusty olivine-bearing chondrules carried the LCb overprint, which was fully removed upon AF application to 20 mT. To summarize, all samples >1.0 mm from the fusion crust, which include all dusty olivine-bearing chondrules, do not carry any post-accretional remagnetization other than the LCa, MCa, and LCb components. These overprints, if present, are readily identified and removed via AF cleaning.

Eight dusty olivine-bearing chondrules were subjected to AF and thermal demagnetization up to 290-420 mT or 780˚C. Six of these were found to carry a high coercivity (HC) or high temperature (HT) component of magnetization. We argue based on seven lines of evidence that these HC/HT components are pre-accretional TRMs (supplementary text). First, HC/HT components decay to the origin upon demagnetization, which is the expected behavior of primary magnetization (Fig. 2). Second, the HC/HT magnetization directions in the six chondrules are collectively random, passing the conglomerate test at the 95% confidence level [Fig. 3; (*27*)]. No HC/HT component is oriented in the direction of any of the post-accretional overprints. Third, the HC magnetizations in chondrules DOC3 and DOC4, which were each partitioned into two subsamples, are unidirectional within each chondrule and inconsistent with random magnetizations at the 99% confidence level. Such uniformity is expected of a TRM acquired by individual chondrules cooling in the solar nebula because the field should be uniform across the submillimeter scale of each sample (*13*). Fourth, the blocking temperature range of the HT component (350-750˚C) agrees closely with that expected of a pre-accretional magnetization that was partially demagnetized for ~5 My at ~200˚C [Fig. 2B; (*15, 18*)], which is the estimated metamorphic temperature for Semarkona on the LL parent body (*15, 24*). Fifth, magnetic field maps of dusty olivine-bearing chondrules confirm that the HC magnetization is carried by dusty olivines, which formed in the nebula and are expected to retain pre-accretional magnetization as outlined above. Sixth, the magnetization direction acquired during cooling for a spinning chondrule is expected to be parallel to its rotation axis (*28*). The close alignment between the HC directions and the short axes of our chondrules, which are likely related to the rotation axis (supplementary text), are non-random at the 98% confidence level, suggesting that

HC/HT magnetizations were indeed acquired parallel to the spin axis. Seventh, the coercivity spectrum of the HC component of dusty olivine-bearing chondrules is very similar to that of an ARM and dissimilar to that of an IRM, which suggests that the HC component was acquired as a TRM (*29*). We therefore conclude with high confidence that the HC/HT magnetizations observed in dusty olivine-bearing chondrules are TRMs acquired in the solar nebula.

TRM acquisition experiments on analogs of dusty olivine chondrules have shown that the ARM normalization method potentially produces paleointensities accurate to ~40% [2σ; (*29*)]. Assuming that the five chondrules with recovered paleointensities formed in similar magnetic field conditions in the nebula, our nominal ARM paleointensities for six dusty olivines yielded a mean value of 27 μT. The morphology of chondrules (*30*) and the apparent correspondence between HC magnetization directions and the short axes of our chondrule samples (see above paragraph) strongly suggest that chondrules were rotating during remanence acquisition in the solar nebula. In the case of rotation around a single axis, which is the expected motion inherited from cooling of a viscous droplet, the true mean field intensity should have been greater than our experimental paleointensity by a factor of 2 (supplementary text). Meanwhile, precession of the chondrule's rotation axis would imply a multiplicative factor of up to 4. However, given the high inferred rotation rates of chondrules (>50 s^{-1}), the magnitudes of effects that may lead to precession are comparatively small. Therefore, we adopt non-precessing rotation as the most likely state of cooling chondrules and recommend a value of 54 ± 21 μT (2σ) for the ambient nebular field strength. Although unlikely, if chondrules did not rotate or precessed strongly during remanence acquisition, the corresponding estimated ambient field strength would be 27 ± 8 μT or 108 ± 42 μT (2σ), respectively.

This paleointensity constrains the magnetic field environment during the last time the chondrule cooled through the 765-350˚C blocking temperature range of the HC/HT component, which likely was the chondrule forming event. Our recommended paleointensity is significantly lower than the >80-400 μT expected for chondrules purportedly formed in the x-wind model (*9*). Furthermore, mechanisms that invoke intense electric currents such as magnetic reconnection flares and current sheets predict strong fields in excess of 500 μT during chondrule heating (*31*). The short circuit instability may also imply similarly strong fields at high temperature (*32*), although the decay of field strength below 765˚C has not been studied in detail. In contrast, given that magnetic fields inherited from the collapsing molecular cloud were likely on the order of 10 μT (*11*), nebular shocks, which may enhance the ambient magnetic field by a factor of <10, would result in paleointensities of <100 μT (*10*). Meanwhile planetesimal collisions would likely not perturb the background field. Therefore, nebular shocks and planetesimal collisions are the chondrule formation models most consistent with our measured paleointensities.

Adopting nebular shocks and planetesimal collisions as the most likely origins of chondrules, background magnetic fields in the nebula may have been amplified by a factor between 1 and 10 during chondrule formation. We therefore infer that background magnetic fields in the solar nebula were between 5 and 54 μT (*10*). Assuming Semarkona chondrules formed near 2.5 AU, which is the present day location of S-type asteroids (*33*), the vertical distribution of dust in the nebula strongly suggests that chondrule formation took place in the weakly ionized "dead zone", which contains gas poorly coupled to local magnetic fields and occurs within ~3 gas scale heights of the midplane (*34*). Our measurements therefore indicate that a substantial magnetic field [yet still well below the ~400 μT equipartition field strength (*3*)] existed in the dead zone, potentially due to fields inherited from the collapse of the solar system's parent molecular cloud. Given our measured field strengths, mass accretion driven by the MRI or magnetic braking at 2.5 AU would have been <0.04-3.5×10^{-8} M_{sun} yr^{-1}, where M_{sun} is the Sun's mass (supplementary text). Meanwhile, the MCW model would predict mass accretion rates of 0.3-30×10^{-7} M_{sun} yr^{-1} or less. The inferred age of Semarkona chondrules is 2-3 My after the first calcium alunimum-rich inclusions (*35*). Given that protoplanetary disks are observed to have accretion rates of 10^{-9}-10^{-7} M_{sun} yr^{-1} at 2-3 My after collapse of their parent molecular clouds (*2*), both magnetic mechanism could fully account for the expected accretion rates. This suggests that magnetic fields govern the observed rapid transformation of protoplanetary disks into planetary systems around sun-like stars.

Acknowledgments

We thank A.J. Brearley, H. C. Connolly, A. M. Hughes, B. C. Johnson, J.L. Kirschvink, M. Mac Low, G.J. MacPherson, M.I. Petaev, D.D. Sasselov, H. E. Schlichting, J.B. Simon, N. Turner, and B. Zanda for a range of discussions that improved the manuscript. We also thank J. Gross, S. Wallace, and Z.I. Balogh for help with SEM and STEM sample analyses and acknowledge S.-C.L.L. Lappe, N.S. Church, S. Russell, M. Uehara, and N. Nakamura for pioneering work on the magnetism of dusty olivines. We thank Thomas F. Peterson for supporting critical instrumentation and analysis costs. R.R.F., B.P.W., E.A.L., S.J.D., and C.S. thank the NASA Origins Program, R.R.F. thanks the NSF Graduate Research Fellowship Program, and C.S. thanks the NASA Lunar Science Institute and the NASA Solar System Exploration and

Research Virtual Institute for support. R.J.H. and T.K. thank the European Research Council under the European Union's Seventh Framework Programme and the Leverhulme Trust for support. X.N.B. acknowledges support from NASA through the Hubble Fellowship. D.G., D.L.S., and R.L.W. thank the DARPA QuASAR program and the NSF for support.

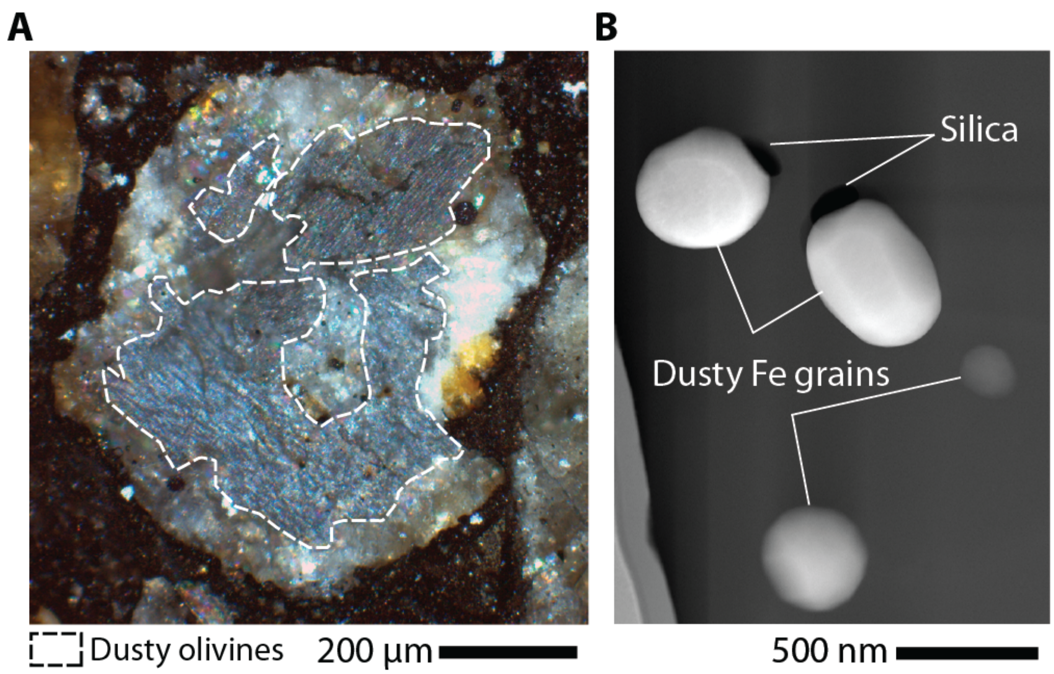

Figure 1. Dusty olivine-bearing chondrules from the Semarkona meteorite. (**A**) Optical photomicrograph of chondrule DOC4 showing the location of dusty olivine grains. Image taken in reflected light with crossed polarizers. (**B**) Annular dark field scanning transmission electron microscope (STEM) image of four dusty olivine Fe grains from chondrule DOC5. Brightness in image reflects column-averaged atomic number; darker grains are smaller in size, implying a higher relative abundance of olivine at their location and hence a lower mean atomic number. Note the euhedral morphology and chemical homogeneity of the Fe grains, which indicate the lack of secondary recrystallization and alteration. Such Fe grains are the primary carriers of pre-accretional magnetization in Semarkona chondrules.

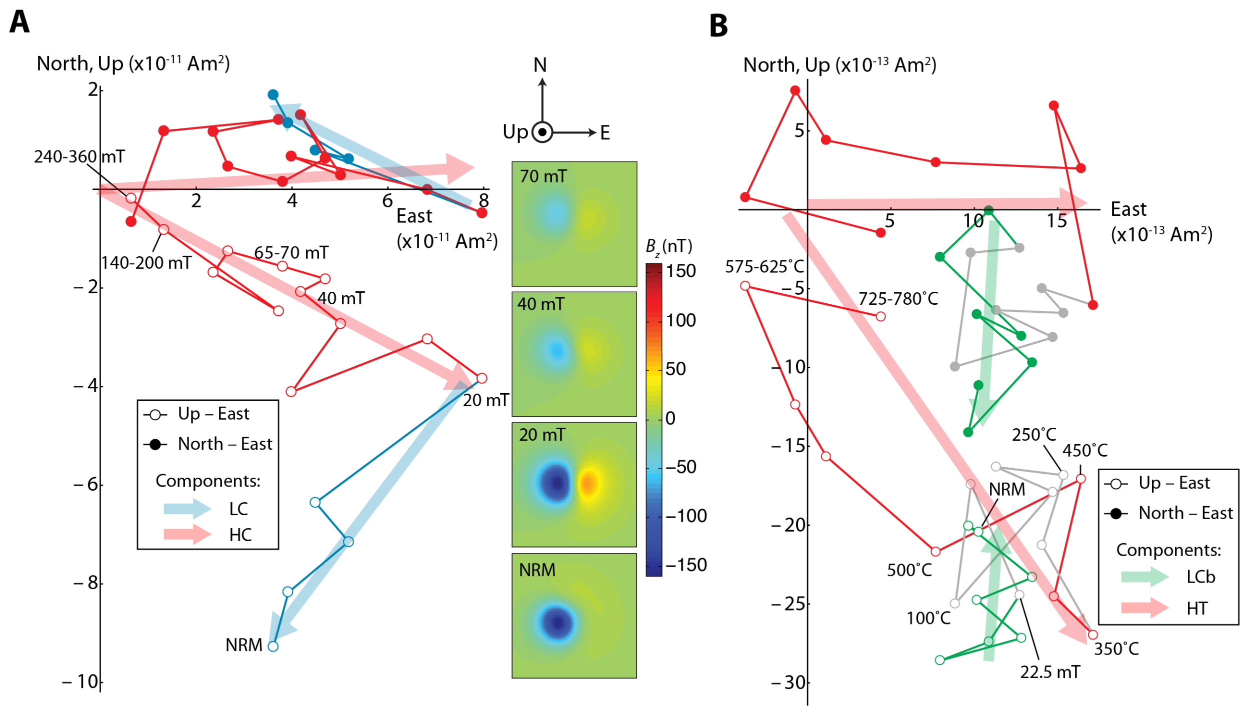

Figure 2. AF and thermal demagnetization of single dusty olivine-bearing chondrules measured using SQUID Microscopy. Orthogonal projection diagrams showing the evolution of the natural remanent magnetization (NRM) of two chondrules upon progressive demagnetization. Open and solid circles indicate the projection of the NRM vector onto the vertical (up-east) and horizontal (north-east) planes, respectively. (**A**) AF demagnetization of DOC1 reveals a low coercivity (LC) overprint removed by 20 mT and higher coercivity (HC) magnetization that persists to >290 mT while decaying in magnitude towards the origin. Insets show associated magnetic field maps measured with the SQUID microscope at the indicated demagnetization levels where positive (red) field values are in the up direction. Note the stable directionality and steady decay of the magnetization during AF application above 20 mT. (**B**) Mixed AF and thermal demagnetization of DOC8 shows the removal of the post-accretional LCb overprint by 20.0 mT (green points), a stationary moment between room temperature and ~400˚C (gray), and an origin-trending high temperature (HT) component removed by 780˚C (red). Steps above 40 mT or 575˚C have been averaged to suppress noise.

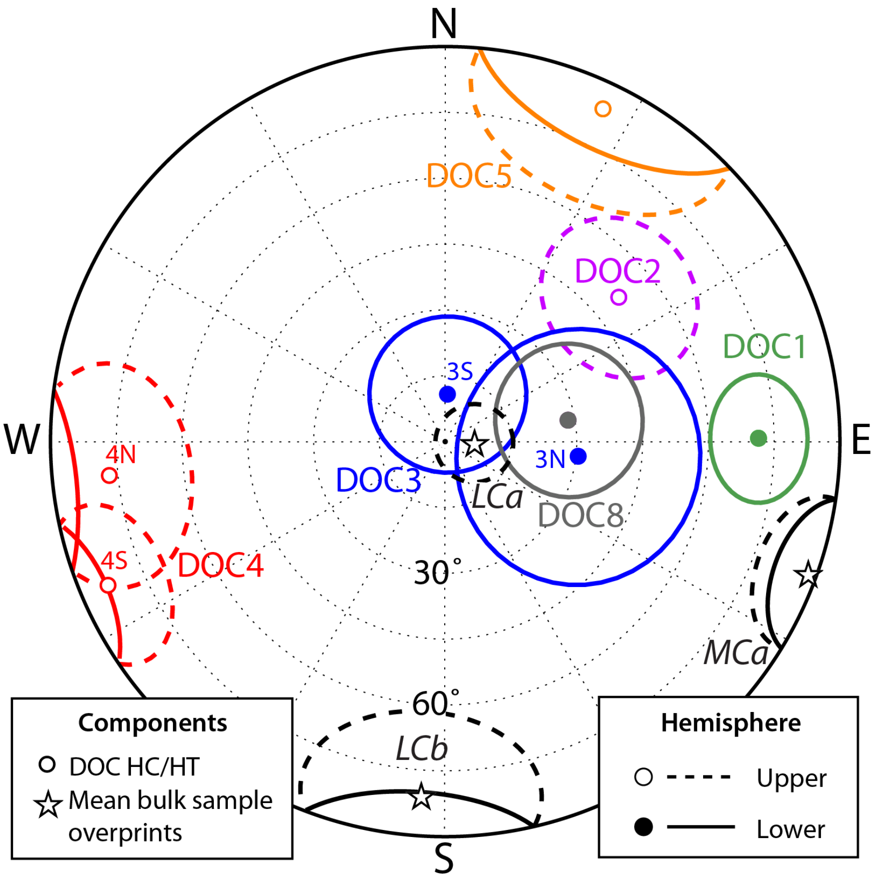

Figure 3. Magnetization directions in Semarkona chondrules and bulk samples. Equal area stereonet projection diagram where colored points and circles denote high coercivity or high temperature (HC/HT) magnetization in individual dusty olivine-bearing chondrule samples or subsamples and the associated maximum angular deviation (MAD) obtained from principle components analysis. Each color represents a single chondrule with chondrules DOC3 and DOC4 having two subsamples each. Black stars and associated ovals represent the mean directions of the three post-accretional overprints identified from bulk samples and their 95% confidence intervals. Open symbols represent the upper hemisphere; solid symbols represent the lower hemisphere. The wide scatter of the HC/HT magnetizations, the unidirectionality of subsamples from DOC3 and DOC4, and their non-correspondence to the directions of post-accretional overprints provide strong evidence for a pre-accretional origin of the HC/HT magnetizations in dusty olivine-bearing chondrules.

Supporting Material for

Solar nebula magnetic fields recorded in the Semarkona meteorite

R. R. Fu*, B. P. Weiss, E. A. Lima, R. J. Harrison, X.-N. Bai, S. J. Desch, D. S. Ebel, C. Suavet, H. Wang, D. Glenn, D. Le Sage, T. Kasama, R. L. Walsworth, A. T. Kuan

*To whom correspondence should be addressed. Email: rogerfu@mit.edu

This PDF file includes:

Supplementary Text
Figs. S1 to S12
Tables S1 to S4
References 1-124

1. Previous searches for nebular magnetic fields

The possibility that chondrules in primitive meteorites could constrain nebular magnetic fields has been recognized previously. Lanoix et al. (*36*) found that isolated chondrules from the Allende CV carbonaceous chondrite carry a strong component of magnetization blocked above 330˚C. They concluded that the apparent paleointensity of this magnetization, which ranged up to 1600 μT, provides evidence for very strong fields in the solar nebula. However, because the Lanoix et al. (*36*) study measured unoriented chondrules, the authors were unable to demonstrate a pre-accretional origin for the observed magnetization (see Section 3.4). In fact, the very high paleointensities and the failure of later experiments to duplicate these results strongly indicate that the purported pre-accretional magnetization component studied in Lanoix et al. (*36*) was due to contamination by strong artificial magnetic fields (e.g., from hand magnets) and does not offer constraints on nebular magnetic fields (*37, 38*).

Two later studies by Sugiura et al. (*12, 39*) of mutually-oriented Allende chondrules identified a high-temperature component of magnetization blocked above 300˚C with random directions that passes the paleomagnetic conglomerate test. The authors concluded that this magnetization component represents pre-accretional magnetization.

However, no new paleointensity was reported for this component. More importantly, the conglomerate test alone is insufficient for establishing a primary origin for the high temperature chondrule magnetization. Post-accretional recrystallization of magnetic phases in a weak ambient field may result in the acquisition of random magnetizations at sub-chondrule scales (*40, 41*). A recent paleomagnetic study of Allende chondrules showed that high temperature magnetization directions among *subsamples* of single chondrules are randomly oriented, ruling out a pre-accretional TRM origin for this magnetization component (*13*). Furthermore, petrographic studies of Allende show that all magnetic phases likely formed during aqueous alteration on the parent body (*42-47*). Therefore, the heterogeneity of the high temperature magnetization in Allende at the sub-chondrule scale suggests that it is instead a crystallization remanent magnetization (CRM) acquired during formation of magnetic phases in a weak to null field on the CV parent body (*13*). This precludes the retention of any pre-accretional magnetization in Allende.

A number of theoretical studies have cited paleointensities of ~100 μT to >1000 μT as experimental constraints of nebular magnetic fields from the Allende studies noted above [e.g., (*9-11, 31, 48-50*)]. However, these paleointensities correspond to a low temperature, post-accretional component of magnetization removed below 300˚C (*37, 51*) or to magnetization found in unoriented chondrules likely exposed to strong artificial fields as described above (*39*). Such paleointensities, because they are derived from post-accretional components of magnetization, offer no constraint on the magnetic field in the solar nebula.

In the case of ordinary chondrites, Funaki et al. (*52*) conducted paleomagnetic experiments on separated chondrules from the L6 chondrite ALH-769. These authors found widely scattered NRM directions in chondrules and suggested that they recorded nebular magnetic fields. However, subsequent paleomagnetic work on ordinary chondrites has shown that chondrule magnetizations in high petrologic grade specimens have been strongly overprinted by the post-accretional formation of tetrataenite, which results in random magnetizations at the sub-chondrule scale and may lead to a false-positive conglomerate test (*41*). Moreover, the >1000˚C estimated metamorphic temperature of type 6 chondrites (*53*) imply that ALH-769 cannot retain pre-accretional magnetization.

Meanwhile, astronomical observations of T Tauri stars allow the measurement of strong magnetic fields within several radii of the central star by observing the Zeeman splitting of stellar absorption lines (*54-56*). Because magnetic fields in the protoplanetary disk are orders of magnitude weaker than the ~0.1 T fields detected near the central star, Zeeman splitting observations of protoplanetary disk fields are limited to low-density regions, which are sampled by lower-frequency lines that can be measured with sufficient signal-to-noise ratio (*57*). As a consequence, Zeeman splitting observations in thermal emission lines are currently limited to H_2 number densities $<10^{12}$ m^{-3} [from CN lines; (*58*)]. Masers, due to their high intensity, can effectively sample higher-density regions with H_2 number density $<10^{17}$ m^{-3} (*6*). Assuming a minimum mass solar nebula (MMSN) (*59*), such densities occur at several scale heights above the accretion disk midplane at 1 AU or in the midplane at large radii (>25 AU) from the star. Higher mass nebula models would place these densities even farther from the midplane and at greater orbital radii. Finally, polarimetry of molecular clouds can detect the alignment of dust grains, which, combined with knowledge of local turbulence and gas density, may be used to estimate magnetic field strength (*60*). However, these estimates require spatially resolved maps of local grain polarization direction, which currently limits magnetic field strength measurements to averages across >100 AU scales [e.g., (*61*)], although future observations using the Atacama Large Millimeter Array (ALMA) can potentially provide field strength estimates at smaller scales relevant to the protoplanetary disk (*62*).

In summary, previous paleomagnetic experiments have been unable to isolate pre-accretional magnetization while astronomical observations of protoplanetary disks cannot currently constrain the magnetic field strength in the planet-forming regions. This motivates the present effort to identify and characterize pre-accretional remanence in chondrules that, unlike those in Allende, escaped significant post-accretional remagnetization.

2. The Semarkona meteorite

2.1. Petrography and thermal history. Since its observed fall and recovery in 1940, the Semarkona LL3.00 chondrite has been studied intensively due to its rarity as an ordinary chondrite that has experienced the mildest metamorphic heating and aqueous alteration on its parent body. As described in the main text, the mild metamorphism of Semarkona to less than 200-260˚C (*23, 24*) and the lack of significant aqueous alteration or strong shock implies that any pre-accretional magnetization should be isolated upon thermal demagnetization to ~450˚C.

Even so, not all magnetic carriers in Semarkona chondrules may retain pre-accretional magnetization. The Ni content of most FeNi metal in ordinary chondrites ranges between 5 and 30% (*63, 64*). Metal grains with such Ni concentrations exist as metastable martensite (α_2-FeNi) after their rapid cooling following chondrule formation (*19, 65*). Subsequent metamorphic heating on the parent body, even to the extent observed in type 3.0 ordinary chondrites, is sufficient to cause exsolution into kamacite (α-FeNi) and taenite (γ-FeNi), which leads to the plessite texture (*66*). Such recrystallization likely leads to the loss of pre-existing magnetization, especially as the transformation from taenite to kamacite involves a change of lattice symmetry from fcc to bcc (*67*). Ni-rich (>5.7 wt%) metal grains in Semarkona have been observed with plessitic exsolution textures while metal grains with lower Ni content are within the kamacite stability field and have been observed to be homogeneous with no sign of recrystallization (*65, 66*). Pre-accretional magnetization, if preserved in Semarkona chondrules, is therefore expected to be carried by grains with <5.7 wt% Ni, which are stable against plessitic exsolution.

Previous petrographic studies of dusty olivine metals have shown that they contain <2 wt% Ni, placing them well within the kamacite stability field and precluding plessitic exsolution (*68*). Furthermore, previous transmission electron microscopy (TEM) imaging of dusty olivine metal grains has revealed no exsolution textures (*14*).

To confirm the low Ni content of dusty olivine metal grains used in our paleomagnetic experiments, we used energy dispersive spectroscopy (EDS) on a scanning TEM to map elemental composition on a ~900×1900 μm area of sample DOC5 that contains three dusty metal grains (Fig. S1). All paleomagnetic measurements were completed prior to these petrographic experiments. We used a FEI Titan 300 kV STEM housed in the Center for Nanoscopy at the Technical University of Denmark. Maps of the elements Fe, Ni, Mg, Si, and O confirm that dusty metal grains contain Fe with <1 wt% Ni and no plessitic exsolution textures. At the same time, the surrounding olivine is essentially pure forsterite with <1 wt% Fe content, which is in agreement with previous studies of dusty olivine compositions (*14*).

Furthermore, to confirm the higher Ni contents of non-dusty olivine metals, we performed quantitative analyses of larger metal grains in the mesostasis of the same chondrule using wavelength dispersion spectroscopy (WDS) on the electron microprobe at the Department of Earth and Planetary Science of the AMNH. We analyzed two large 10-100 μm FeNi grains, which have Ni contents of 0.8 and 7.9 wt%, signifying that mesostasis metal grains span a wide range of compositions. Metal grains with compositions similar to the latter analyzed Ni-rich grain are capable of undergoing plessitic exsolution, which may occur at scales smaller than the ~3 μm resolution of our image on the electron microprobe (*19*).

In summary, petrographic observations show that dusty olivine metals in Semarkona chondrules have escaped recrystallization since their initial formation during chondrule heating in the solar nebula. While some mesostasis metal may have experienced plessitic exsolution, dusty olivine metals are expected to have escaped all significant post-accretional remagnetization effects and should retain pre-accretional magnetization blocked above ~450˚C. We therefore focus on paleomagnetic data derived from isolated dusty olivine-bearing samples to constrain pre-accretional magnetic fields.

2.2. Domain state of ferromagnetic minerals. Previous TEM-based studies of dusty olivine-bearing chondrules have reported <100 nm metal grains, which are likely in the single domain

(SD) state. Most grains, which are one to several 100s nm in diameter, likely exist in the single vortex (SV) state (*14, 16*). AF demagnetization of our dusty olivine-bearing chondrules (see Section 3.3) shows that seven out of nine samples carry high coercivity magnetization that remains stable above 170 mT, indicating the presence of SD metal grains [Table S1; (*29*)].

We directly confirm the presence of both SD and SV metal grains in our dusty olivine-bearing chondrules. After the completion of all paleomagnetic measurements, we imaged sample DOC4S using the secondary electron detector on a Zeiss NVision40 scanning electron microscope (SEM) housed at the Harvard Center for Nanoscale Systems (CNS). These images revealed the presence of ~60 nm, likely SD metal grains (Fig. S2A). Finally, we obtained electron holograms of several dusty olivine metal grains from sample DOC5 (see above for analytical details), which showed that the majority of visible grains are in the SV state, with only the largest grains (>300 nm) existing in the multi-domain (MD) state (Figs. 1B, S2B,D). We therefore conclude that the primary magnetic carriers in our dusty olivine-bearing chondrules are SD and SV kamacite grains, which are expected to retain magnetization over the age of the solar system (*17, 18*).

3. Paleomagnetic measurements

3.1. Sample extraction and measurement. All paleomagnetic measurements were performed on samples extracted from two 15 mm × 10 mm × 150 μm slices of Semarkona designated ps8 and ps3. Both slices were cut from the main sample of Semarkona at the AMNH called AMNH 4128-t4. The slices are separated by a distance of ~0.9 mm. We used a Princeton Scientific Corp. Model WS22 wiresaw at the AMNH with a 50 μm diameter tungsten wire and boron carbide-based cutting fluid to cut each slice from the main sample. Measurement of a single drop of boron carbide cutting fluid in the 2G Enterprises Superconducting Rock Magnetometer (SRM) showed that the magnetic moment is $<10^{-12}$ Am^2, which is the detection threshold of the SRM. Each surface of the Semarkona slices was then lightly polished with 600 grit, alumina-based sandpaper to flatten the surfaces for optical imaging (see below). Both slices were then washed with acetone and mineral spirits in an ultrasonic cleaner to remove all residual material from the cutting and polishing process.

Each slice was then glued using non-magnetic cyanoacrylate cement to ~150 μm thick GE124 quartz coverslips. We use the MIT SQUID Microscope, which acquires high-sensitivity maps of the vertical component of the magnetic field above the surface of samples with spatial resolution of ~200 μm and noise threshold of 10 to 100 pT (*25, 69*), to confirm that these coverslips are magnetically clean and contain no contamination with magnetic moment greater than $\sim 10^{-15}$ Am^2. Reflected light optical microscopy was then used to image both sides of each Semarkona slice, permitting the identification of chondrules suitable for extraction (Fig. S4). Except during the cutting, polishing, and extraction procedures, all samples were kept in the magnetically shielded room of the MIT Paleomagnetism Laboratory with DC fields <150 nT.

All extraction and measurement of paleomagnetic samples from the Semarkona slices were carried out at the MIT Paleomagnetism Laboratory. We used a degaussed, tungsten-carbide dental scriber mounted on an Electro Scientific Industries Inc. Micromill to excise samples from surrounding material (Fig. S3). In the case of chondrule extractions, we took care to fully remove metal and sulfide-rich rims, which suffered aqueous alteration on the LL parent body and may carry secondary magnetization (*23, 70*). In the case of dusty olivine-bearing chondrules, we also removed large visible mesostasis metal grains, although some small mesostasis metal grains remain in all dusty olivine-bearing chondrules due to their inaccesible location in the samples. For the dusty olivine-bearing chondrules DOC3 and DOC4, we cut each chondrule into two subsamples to perform the unidirectionality test for pre-accretional TRM (see Section 3.4). SQUID Microscope scans on sample slices before and after cutting show that this process does not introduce detectable spurious magnetization.

Masses of larger samples were measured directly on a Mettler Toledo electronic scale with ~0.05 mg effective precision. Chondrule masses below the reliable measurement threshold of the electronic scale were estimated using photographically determined volumes and an assumed density of 3300 kg m^{-3} to approximate the single-grain density of olivine. For all samples, photomicrographs taken of the extracted samples were referenced to those taken of the whole Semarkona slice before extraction, permitting mutual orientations to <5˚.

In the case of bulk samples, which have greater masses and higher magnetic moments (Table S2), we mounted the extracted samples to 3 mm GE124 quartz rods with magnetic moments of less than 2×10^{-12} Am^2 using cyanoacrylate cement and measured their magnetic moments using the SRM. The sample holder moment of 2×10^{-12} Am^2 represents the effect noise level of these measurements. All samples measured using the SRM have NRM moments of greater than 10^{-10} Am^2 to maintain a high signal-to-noise ratio upon demagnetization.

For chondrule samples, which usually have NRM moments below 10^{-11} Am^2, we mounted the extracted samples on magnetically clean GE124 quartz disks using cyanoacrylate for measurement using the SQUID Microscope. We mapped the magnetic field at a sample-sensor distance of 250-350 μm. To better isolate the dipolar component of sample magnetization, we first performed a bilinear interpolation of the field map by a factor of 4 in each horizontal direction and upward continued the field map to achieve an effective sensor-sample distance of 450-550 μm (*71*). We then modeled the upward continued magnetic field using a non-linear optimization algorithm that adjusts the model magnetic moment (direction and magnitude) and sample location to find the sample magnetization that best reproduces the observed field maps. This technique for the recovery of magnetic dipole moment has been tested on both terrestrial and extraterrestrial samples, including chondrules from the Allende CV chondrite (*13, 72*). In both cases, SQUID microscope-recovered moments of samples sufficiently strong to be measured on the SRM agreed closely with measurements conducted with the SRM.

Finally, we used NV quantum diamond magnetic imaging (*73*) to map directly the spatial distribution of magnetic sources that contribute to the magnetization of dusty olivine-bearing sample DOC1. The magnetic sensing element was a 2.5 × 2.5 × 0.5 mm diamond chip, grown by chemical vapor deposition and engineered to contain a dense surface layer of nitrogen-vacancy (NV) color centers (estimated density ~ 3×10^{11} NV/cm^2 in a ~10 nm thick layer at a mean depth of ~20 nm below the diamond surface). This diamond surface was mounted above the sample with a standoff distance of ~20 μm. We acquired images of all three vector components of the magnetic field produced by the sample in the plane of NV sensors using optically-detected magnetic resonance (ODMR) spectroscopy. In this technique, described by Le Sage et al. (*74*), the magnetic field is determined from the resonance frequencies of the NV electronic spin-flip transitions $|m_s = 0\rangle \leftrightarrow |m_s = \pm1\rangle$, which are measured by scanning the frequency of a continuous microwave drive field while monitoring spin-state dependent changes in NV fluorescence that is excited by a low intensity (<240 W/cm^2) laser beam at 532 nm with spot dimensions of approximately 1000 by 400 μm. We imaged the NV fluorescence onto a sCMOS camera, allowing magnetic fields in the plane of the NV sensing layer to be mapped with a spatial resolution of ~1 μm. To spectrally resolve spin-flip transitions of NV centers oriented along different diamond crystal axes, we applied a 1.27 mT magnetic bias field using three orthogonal sets of Helmholtz coils. We were able to distinguish fields generated by remanence-carrying grains from those of soft paramagnetic or superparamagnetic components by carrying out a second measurement with the bias field precisely reversed and summing the field maps measured in each case. We measured the bias reversal precision in a region of the sensor far from the sample, and determined it to be $< 2\times10^{-3}$ of the mean bias field, which was sufficient to cancel all paramagnetic components of the observed signal to below the magnetic noise floor of these measurements, which is ~0.08 μT.

3.2. NRM of bulk samples. We extracted a total of 29 bulk samples with masses between 0.08 and 0.59 mg to characterize any post-accretional overprints in our Semarkona samples (Fig. S4; Table S2). We performed stepwise three-axis AF demagnetization up to 85 mT on 22 samples and up to 145 mT on 5 samples. All bulk samples were fully demagnetized by 85 mT. We demagnetized samples in 0.5 mT steps below 25 mT, in 1 mT steps between 25 and 100 mT, and in 2-2.5 mT steps between 100 and 145 mT. We applied the AF and measured the sample moment three times at each field level during AF demagnetization to suppress noise. We then fitted the direction of magnetization components using principal component analysis (PCA) (*75*).

Three samples subjected to AF demagnetization contained fusion crust material while the remainder were separated from the fusion crust by distances between 0.8 and 11.4 mm. We subjected one sample 1.9 mm from the fusion crust (m6) to stepwise thermal demagnetization up to 580˚C.

To aid in identifying the origin of each post-accretional overprint, we obtained IRM normalized paleointensities on 11 bulk samples by first applying a 280 mT IRM to the bulk sample and then performing stepwise AF demagnetization up to 85 or 145 mT. The IRM paleointensity for each magnetization component was then calculated using the equation (*76*):

$$B_{IRM} = a\frac{\Delta NRM}{\Delta IRM} \quad (1)$$

where B_{IRM} is the paleointensity, ΔNRM is the vector-subtracted change in the NRM magnitude in the component's AF interval, ΔIRM is the moment lost from the IRM demagnetized through the same AF range, and a is the ratio between a saturation IRM and a low-field TRM in the relevant coercivity range. In the absence of TRM acquisition experiments on Semarkona bulk samples, we adopt a value of $a=3\times10^3$ (*76*), which is typical of metal-bearing samples.

We obtained ARM normalized paleointensities for 11 bulk samples by first imparting an ARM in a 280 mT AC field and a 50 μT bias field. We then subjected each sample to stepwise AF demagnetization up to 85 or 145 mT. The ARM paleointensity for each component was then given by (*77*):

$$B_{ARM} = f^{-1} B_{bias} \frac{\Delta NRM}{\Delta ARM} \quad (2)$$

where B_{ARM} is the paleointensity, B_{bias} is the bias field of the laboratory ARM, ΔARM is the ARM moment acquired in the same AF range as the NRM component, and f is the ratio between the moment of a TRM and that of an ARM acquired in the same bias field. As was the case for the IRM calibration factor a, the value of f has not been determined for Semarkona bulk material using TRM acquisition experiments. We adopt f=1.34 as a typical value for metal-bearing samples (*78, 79*).

Both a and f are subject to uncertainties of a factor of 3-5 (*21, 80*). Because the paleointensities of bulk samples are used only as an aid towards determining the origin of post-accretional overprint, uncertainties in the paleointensities within this range do not affect our conclusions. Paleointensities for dusty olivine-bearing chondrules, which we use to constrain nebular magnetic field strength, are subject to much smaller uncertainties (see Section 4.1).

3.2.1. The LCa component. AF and thermal demagnetization of both fusion crust and interior samples revealed a unidirectional LCa component of magnetization blocked up to 11.5 mT or 70°C in 20 out of 29 bulk samples (Figs. S5 and S6A). Where observed upon thermal demagnetization in sample m6, we call this component LTa (Table S2). The presence of the LCa component in these samples regardless of their distance to the fusion crust indicates that the component was acquired after arrival on Earth, while its low unblocking temperature indicates that it is likely a VRM. The mean paleointensity of this component is 94 μT, which is within uncertainty of the terrestrial field strength of ~50 μT. The dominant ferromagnetic phases in the matrix and chondrules rims in Semarkona and similar unequilibrated LL chondrites are kamacite, magnetite, maghemite, Ni-rich metal, and possibly sulfides (*23, 81*). Assuming that the LCa component is carried primarily by single domain pyrrhotite, the demagnetization of this component by 70˚C is consistent with exposure to a stable Earth-strength magnetic field at 20˚C for several decades (*51*), such as that expected during long-term storage. If the LCa component is primarily carried by magnetite, maghemite, or FeNi metal, the observed demagnetization temperature would imply storage of <1 year (y) at 20˚C (*18, 82*), which may represent the most recent period of undisturbed storage at the AMNH. Either scenario would be consistent with the acquisition of the LCa magnetization during the meteorite's curation since 1940.

3.2.2. The MCa component. Fourteen out of eighteen samples located 4.7 mm or less from the fusion crust carry the unidirectional MCa overprint while zero out of thirteen samples farther from the fusion crust carries this component. This spatial distribution demonstrates that the MCa magnetization is the result of atmospheric heating in the geomagnetic field. The nearest interior sample to the fusion crust that did not carry the MCa component is m4, which is 0.8 mm away. This implies that all chondrule samples, which were extracted >2.0 mm from the fusion crust, likely carry no MCa component. The heterogeneity of the presence and strength of the MC component between 0.8 and 4.7 mm from the fusion crust may be due to uneven conduction of atmospheric heating into the meteorite interior, which is consistent with the mixture of both non-porous chondrules and porous, insulating matrix. Alternatively, the MCa component may be a thermochemical remanent magnetization (TCRM), whose acquisition varied with the local composition of magnetic phases. Finally, the blocking temperature spectrum of bulk samples may be significantly lower than that of chondrule samples, allowing the recording of a low temperature thermal overprint. Such low blocking temperatures would be consistent with the presence of pyrrhotite in the matrix (*23*), which has much lower blocking temperatures compared to those of FeNi metal in chondrules.

The mean paleointensity of 76 μT is also consistent within error with the geomagnetic field. Thermal demagnetization shows that sample m6, which is 1.9 mm from the fusion crust, carries a MCa/MTa component blocked up to 220˚C, which is consistent with heating during atmospheric passage based on thermoluminescence studies of ordinary chondrites (*83*). In comparison, all chondrule samples were extracted further from the fusion crust than sample m6. For any chondrule sample that carries the MCa component, the atmospheric heating it experienced was therefore likely lower than 220˚C. Therefore, all chondrule samples were heated to a lower temperature during atmospheric entry than during metamorphism on the LL parent body, implying that atmospheric heating did not contribute to the removal of pre-accretional remanence in extracted chondrules.

Seven bulk samples taken from <0.9 mm from the fusion crust contained additional strong components of magnetization. These magnetizations were non-unidirectional across the bulk samples. We therefore label these components as "U" for "unpaired" in Table S2. Due to the closeness of these samples to the fusion crust, we interpret them as TRMs acquired during tumbling of the meteorite during atmospheric entry. In contrast, the MCa component, which penetrated to much greater depths from the fusion crust, was likely acquired during a longer time window during atmospheric entry when the attitude of the meteorite was stable with respect to the Earth's field. As in the case of the LCa and MCa components, the mean paleointensity of U components (70 μT) is consistent with the geomagnetic field. Because all chondrule samples were extracted at least 2.0 mm from the fusion crust, these samples are not expected to carry any U components.

3.2.3. The LCb overprint. Finally, five bulk samples near the southern edge of both ps3 and ps8 slices between 4 and 11 mm from the fusion crust carry a unidirectional LCb overprint blocked between 0 and 6.5-30 mT. The very high NRM to saturation IRM ratio of this component (0.23) indicates that it is an IRM acquired during exposure to artificial fields. The maximum unblocking coercivity suggests that the artificial field had a maximum intensity of ~30 mT (*84*), which is consistent with a weak hand magnet (*38*). Furthermore, the presence of the LCb overprint only in samples from local area within 2 mm of the sample edge is expected for an origin due to contact with a hand magnet. Two chondrules (DOC5 and DOC8) were extracted from the area carrying the LCb magnetization. AF demagnetization of DOC5 and adjacent bulk sample m29 showed that the LCb component was fully removed by 15 mT and 16 mT, respectively. We performed AF demagnetization of DOC8 up to 22.5 mT before undertaking thermal demagnetization to remove fully the LCb overprint. The resulting demagnetization sequence shows that the LCb component was completely removed by 20 mT (Fig. 2B). The wide angular separations between the LCb direction and those of higher coercivity and temperature components in both DOC5 and DOC8 confirm that the LCb component was fully removed from these samples.

3.3. NRM of dusty olivine-bearing chondrules. The unique compositional and magnetic properties of dusty olivine metals described in the main text and in Section 2 suggest that dusty olivine-bearing chondrules should retain pre-accretional magnetization. To identify and characterize any pre-accretional magnetization, we extracted eight dusty olivine-bearing chondrules with masses between 0.008 and 0.09 mg.

Due to their small size and weak NRM moments (between 9.9×10^{-11} and 9.4×10^{-13} Am^2) (Table S1), all dusty olivine-bearing chondrules were measured using the MIT SQUID Microscope. Because measurements on the SQUID Microscope are time-intensive compared to those on the SRM, demagnetization sequences for dusty olivine-bearing chondrules are of lower resolution than those of bulk samples. We applied three-axis AF demagnetization in steps of 5 mT up to 90 mT, in steps of between 5 and 20 mT up to 200 mT, and in steps of between 30 and 50 mT above 200 mT. Most samples were demagnetized up to 290 mT while two chondrules with exceptionally high coercivities, DOC1 and DOC4, were demagnetized up to 360 and 420 mT, respectively. We repeated the AF application and measurement up to five times for each AF level above 40 to 90 mT to minimize noise. For demagnetization steps above 25-40 mT, we averaged the moments of two to four adjacent AF levels to suppress noise further (*85*).

We carried out thermal demagnetization on sample DOC8 in 50˚C steps to 550˚C followed by 25˚C steps to 750˚C and a final step at 780˚C. The sample was held at the peak temperature for ~20 minutes during each heating step. To prevent oxidation of the dusty metal grains upon heating, we used a CO_2 and H_2 gas mixture (*86*) to maintain the oxygen fugacity at two to three log units below the iron-wüstite buffer (IW-2 to IW-3), which is near the theoretical equilibrium oxygen fugacity of an olivine crystal with Fa_{10} composition (*14, 87*). We averaged the moment measured in each three adjacent demagnetization steps above 575˚C to suppress noise. Finally, after the completion of the thermal demagnetization sequence, we attempted partial TRM acquisition experiments on the DOC8 sample with a 50 μT bias field at temperatures between 300 and 780˚C. However, apparent sample alteration during heating above 600˚C prevented recovery of high-fidelity partial TRM acquisition sequence. We therefore do not include these experiments in our final paleointensities analyses.

3.3.1. The LCa, MCa, LCb overprints. Among the eight extracted dusty olivine-bearing chondrules, DOC6 was 2.1 mm from the fusion crust while all other samples were located >3.4

mm away. As a consequence, DOC6 was the only chondrule sample that carries the MCa overprint due to atmospheric heating, which is blocked between 50 and 120 mT. The presence of the MCa overprint in DOC6 confirms that the mounting and measurement procedure on the SQUID Microscope did not result in significant contamination or remagnetization. No dusty olivine-bearing chondrules carried the LCa component, likely due to differences in the rate of VRM acquisition between chondrule and matrix material. The difference in magnetic mineralogy between the matrix and chondrule materials can account for large variations in the rate of VRM acquisition (*67*). Finally, as discussed in Section 3.2, the LCb overprint is present in dusty olivine-bearing chondrules DOC5 and DOC8 where it is fully removed by AF demagnetization up to 15 and 20 mT, respectively (Fig. 2B).

3.3.2. The LC component. All dusty olivine-bearing chondrules except DOC5 and DOC8 carry at least one unique low coercivity (blocked up to between 15 and 87.5 mT depending on the sample) component of magnetization oriented in random directions relative to components found in other chondrule and bulk samples. Because these are not directionally consistent with the identified overprint directions LCa, LCb, and MCa, we generically refer to these magnetizations as LC components. All dusty olivine-bearing chondrules carry only one LC component except for the subsamples of DOC4, which carry two randomly oriented LC components (denoted LC_1 and LC_2; Fig. S7 and Table S1). Analogous LC components are also present in some non-dusty olivine-bearing chondrules (NDOC; see Section 3.5), strongly suggesting that LC magnetizations are carried by recrystallized Ni-rich metal grains, which are present in the mesostases of all chondrules. Furthermore, the low coercivity range of these components is consistent with their presence in MD mesostasis metal grains (*22*). As discussed in Section 2.1, the plessitic unmixing of kamacite and Ni-rich taenite phases in such grains during metamorphism on the LL parent body in a weak field likely resulted in the loss of any pre-accretional remanence and the acquisition of randomly oriented, spontaneous magnetizations. Similar secondary magnetizations have been observed in other ordinary chondrites (*40, 41, 88*).

3.3.3. The HC/HT component. Five of seven dusty olivine-bearing chondrules subjected to AF demagnetization carry an HC component of magnetization blocked above any LC components and up to 240-380 mT. The high coercivities above 170 mT indicate that SD kamacite grains are responsible for carrying part of the HC magnetizations (*29*). The field geometry observed in SQUID Microscope and NV diamond magnetometer maps confirm that high coercivity magnetization is carried by dusty olivine grains (Fig. S8).

In contrast to these chondrules that carry HC magnetization, DOC7 carries no directionally stable component above 37.5 mT while DOC6 carries a possible HC component blocked between 100 and 240 mT. However, given that the latter putative component consists of only four averaged demagnetization steps and that an ARM in DOC6 (see below) is fully demagnetized by 100 mT, we do not consider this magnetization to be a reliable HC component. In any event, inclusion of this component's direction in the conglomerate test (see Section 3.4) does not affect the outcome of the test. The absence of a reliable HC component in samples DOC6 and DOC7 may be due to the presence of a higher abundance of unextracted mesostasis metal grains which have very low coercivities and contribute significant noise during AF demagnetization (*89*). Alternatively, these chondrules may have tumbled, possibly due to the loss of angular momentum, during their cooling process and thereby never acquired a unidirectional TRM. Finally, the rotation axis of these chondrules may have been nearly perpendicular to the ambient magnetic field during cooling (see Section 3.4), resulting a very weak effective bias field that did not impart an identifiable remanent magnetization.

All HC components are origin-trending as confirmed by the comparison between the maximum angular deviation (MAD), which describes the uncertainty in the component direction as determined using PCA, and the deviation angle [DANG; (*90*)], which is the angular difference between the best-fit direction of the HC component according to PCA and the vector from the origin to the centroid of data points that make up the HC component (i.e., the best-fit direction of the HC component, assuming that it passes through the origin). If DANG < MAD, then the component's decay is origin-trending to within the uncertainty of the component's direction (*21, 78*). The rate of HC component decay over its coercivity range is similar to that of an ARM but not to that of an IRM (Fig. S9), providing evidence that the HC component was acquired as a TRM (*77*).

The NRM of DOC8 remained stable in both direction and intensity during thermal demagnetization up to 400˚C (Fig. 2B). Rapid decay towards the origin commenced upon heating to 400-450˚C and continued until the loss of directional stability at ~750˚C. The survival of this HT component up to above ~550˚C shows that tetrataenite cannot be its primary carrier

(*91*). The blocking temperature range of this HT component and the lack of component decay below ~400˚C are fully consistent with that expected for a pre-accretional TRM in the chondrule that had been thermally demagnetized in a null field on the LL parent body during 5 My of metamorphism at 200˚C (*15, 18*). The thermal demagnetization sequence of DOC8 therefore offers strong evidence that pre-accretional remanence is preserved in dusty olivine-bearing chondrules.

Because the precise relative directions of the HC/HT components are critical for paleomagnetic tests for a pre-accretional origin (see Section 3.4), we conducted ARM acquisition experiments to compute the anisotropy tensor for all dusty olivine-bearing chondrule samples except DOC8 after the completion of their NRM demagnetization. In the case of DOC8, possible sample alteration during partial TRM acquisition experiments may have affected the anisotropy of the sample (see Section 4.1). For other samples, we isolated the anisotropy tensor most relevant to the HC component by first imparting an ARM in a 290 mT AC field with a 200 μT bias field and then AF demagnetizing the ARM up to the lower bound of the coercivity range of the HC component (*92*). We imparted two such AF-cleaned ARMs to each of three orthogonal axes, measured the resulting remanence using the SQUID Microscope after each application, and averaged the moments from the two applications to compute all six independent elements of the anisotropy tensor. For the dusty olivine-bearing chondrule samples that carry an HC component, the anisotropy ratio *P*, defined as the ratio between the greatest and smallest eigenvalues of the anisotropy tensor, spans a range between 1.4 and 2.5, implying moderate to high degrees of anisotropy (*93*).

We find no evidence of gyroremanent magnetization (GRM) acquired during our AF demagnetization experiments (*84*). The magnitude of GRM associated with a certain orientation of the AF axis and sample is expected to increase with the application of higher AF levels, as more high coercivity magnetic grains would be magnetized by the AF application (*94*). In all cases, the HC magnetization decays uniformly to the origin (see above) without detectable increase in moment in an identifiable direction.

3.4. Statistical analysis of dusty olivine-bearing chondrule data. The relative directions of the HC/HT magnetizations provide critical clues regarding their origin. To test the hypothesis that the HC/HT components are pre-accretional, we perform the paleomagnetic conglomerate test on all dusty olivine-bearing chondrules and the unidirectionality test on subsamples of two individual chondrules. In the conglomerate test, mutually random chondrule magnetization directions support a pre-accretional origin since chondrules likely accreted onto the parent body in random orientations (*27*). In contrast, magnetizations that are unidirectional among different chondrules were acquired after accretion of the meteorite. In the unidirectionality test, coherent magnetization directions found in subsamples of the same chondrule provide evidence for the acquisition of magnetization in a uniform ambient magnetic field [e.g., (*95, 96*)]. A sample that passes both paleomagnetic tests must have chondrules with mutually random but internally unidirectional magnetizations.

Passing both tests provides strong evidence that the chondrule magnetizations are pre-accretional. Samples that pass the conglomerate test alone may have suffered post-accretional remagnetization in a weak-field environment that randomized magnetization at small scales, resulting in a false-positive outcome (*13, 41*). Application of the unidirectionality test eliminates this possibility, as subsamples of weak-field remagnetized chondrules would show mutually random magnetizations. Furthermore, chondrules that pass both paleomagnetic tests likely acquired magnetization as a TRM during cooling in the nebula. Although a CRM can potentially record pre-accretional magnetic fields, no evidence for recrystallization exists in dusty olivine metals (see Section 2.1), precluding a CRM origin for their magnetization.

To perform the conglomerate test, we use the anisotropy-corrected HC/HT component directions recovered from all six dusty olivine-bearing chondrules found to contain these magnetizations. For chondrules DOC3 and DOC4, each of which has two subsamples, we take the mean of the unit vectors representing each subsample's magnetization direction. Because of the close agreement between the magnetization directions within each pair of subsamples (see below), the choice of averaging technique does not affect the result of the conglomerate test. The resulting set of six HC/HT directions passes the conglomerate test at the 95% significance level (*27*). Specifically, a set of six randomly oriented vectors has a 38% probability of showing more unidirectionality than the set of six HC/HT directions, implying that these directions are fully consistent with a random distribution and do not tend toward an identifiable direction.

We use two approaches to evaluate the unidirectionality of HC/HT components found in subsamples of DOC3 and DOC4. First, we test whether the directions for each subsample are consistent with a single magnetization direction in each chondrule given the uncertainties on the component directions. As above, we adopt the mean between the HC component unit vectors for each pair of subsamples as the mean HC direction of each chondrule. For all four subsamples, the angular separation between the subsample HC direction and the mean HC direction of the chondrule is smaller than the MAD of the subsample HC component, implying that the subsample and mean directions agree at the 1σ level (*75*). All subsample HC directions are therefore consistent with the sampling of a single true HC direction in each chondrule.

Second, we compute the probability that the apparent alignment between the HC directions of subsamples from each chondrule occurred randomly. If the HC directions in all subsamples are independent and randomly distributed over the unit sphere, the probability density function (P) for the angular separation (θ) between the HC directions of two subsamples from a single chondrule is given by (*97*):

$$P(\theta) = \frac{1}{2}\sin\theta \tag{3}$$

over the domain $0^\circ \leq \theta \leq 180^\circ$. Because we took two subsamples each from two separate chondrules, we must evaluate the probability that randomly oriented magnetizations resulted in the observed degree of unidirectionality in both chondrules simultaneously. The probability density function (Q) of the sum of the separations between HC directions in both chondrules ($\theta_1+\theta_2$) may be derived from the convolution of Eq. 3 with itself [p. 136 of ref. (*98*)]. The result is a piecewise function that is given by:

$$Q(\theta_1+\theta_2) = \frac{1}{8}[\sin(\theta_1+\theta_2) - (\theta_1+\theta_2)\cos(\theta_1+\theta_2)] \tag{4}$$

over the restricted domain $0^\circ \leq \theta \leq 180^\circ$. The measured separations of subsample HC directions in DOC3 and DOC4 are 32.8° and 17.7° (Table S1), respectively, resulting in $(\theta_1+\theta_2)=50.6^\circ$. Integrating Eq. 4, the probability of two pairs of random directions yielding $(\theta_1+\theta_2)<50.6^\circ$ is 0.0060. We therefore reject the hypothesis that the unidirectionality of the HC component in both subsampled chondrules occurred randomly at the 99% confidence level. A simpler but more restrictive calculation of the joint probability, multiplying the individual probabilities that the angular separation observed in each chondrule is less than the observed value, yields an even lower joint probability of 0.0019.

Because the unidirectionality test is critical to our interpretation of a pre-accretional origin for the HC magnetization, we verify the above calculations by performing Monte Carlo simulations using Mathematica. In each instance of the simulation, we choose four random directions from a uniform distribution on the unit sphere and sum the angular separations between the first pair and between the second pair. In a simulation of 10^6 instances, 5901 or 0.59% resulted in a sum of separations of less than 50.6°, fully corroborating our theoretical calculations. In summary, our statistical analysis of HC/HT directions shows that (1) the mean magnetization directions of the six dusty olivine-bearing chondrules represent a random distribution, (2) the directions of chondrule subsamples from DOC3 and DOC4 are consistent with unidirectional magnetization in each chondrule, and (3) the unidirectionality of these subsample magnetization is non-random at the 99% confidence level. We therefore conclude that the HC/HT components pass both the conglomerate and the unidirectionality test with high confidence, providing strong evidence for a pre-accretional TRM origin of these magnetizations.

As an additional test for pre-accretional origin of the HC/HT magnetizations, we evaluate the correspondence between the direction of magnetization and the inferred spin axis of the chondrules. The shortest principal axis of oblate chondrules may represent the spin axis of the chondrules during cooling near the solidus (*30, 99*). Because spinning objects cooling in a magnetic field acquire a magnetization parallel to the spin axis (*28*), pre-accretional magnetization may be parallel to the shortest physical dimension of the chondrule. We note that our following analysis assumes that the chondrule morphology is indeed a result of rotation instead of, for example, the presence of unmolten relic grains near the surface or to aerodynamic effects (*30*). Furthermore, we assume that the chondrules are rotationally symmetric spheroids although we cannot confirm this given the effectively two-dimensional (2D) sections available to us.

Because we extracted all chondrules from 150 μm thick slices of Semarkona, our samples cannot uniquely define the three-dimensional (3D) orientation of the chondrules' short axis. However, approximating chondrules as oblate ellipsoids of rotation, the section of the chondrule that appears on our sample slice is an ellipse whose orientation constrains the direction of the true, 3D short axis. Specifically, the 3D short axis must lie in a plane that is perpendicular to that of the sample slice and that passes through the short axis of the sectioned ellipse [i.e., the 2D short axis; (*100, 101*)]. Close alignment between the magnetization direction and the 3D short axis would therefore imply a correspondence between the azimuth of the magnetization and that of the 2D short axis of the chondrule section.

Because the plane of the sample slice corresponds to the horizontal plane (i.e., the inclination (i) equals zero plane) in our coordinate system, we compare the anisotropy-corrected declination of the HC/HT components and that of the chondrules' 2D short axes (Fig. S10). To objectively determine the orientation of the latter, we select the Cartesian coordinate of 12 points evenly spaced points on the boundary of the chondrule and use the MATLAB routine `fitellipse` to compute the short axis orientation of the best-fit ellipse (*102*). Following the preceding analysis for the unidirectionality of DOC3 and DOC4 subsamples, we evaluate the unidirectionality of the component declinations and the 2D short axis orientations by calculating the probability that the observed angular discrepancies occurred by chance. If the declinations of the magnetization and short axis are mutually independent, their separation for each chondrule would be uniformly distributed between 0˚ and 90˚ [the short axis has no preferred sense; (*103*)]. Out of six dusty olivine-bearing chondrules that carry an HC/HT component, only three are available for this analysis. Two chondrules are incomplete due to their location at the edge of the sample slices, which precludes an accurate assessment of their shape. One chondrule, DOC3, carries an HC component oriented nearly normal to the slice plane and therefore does not have a well-determined declination. For a sample size of three, the probability density function of the sum of all three separation angles ($\phi_1 + \phi_2 + \phi_3$) may be found by the convolution of the uniform distribution that describes each separation angle [(*98*), p. 136]. Analogously to Eq. 4, the result is a piecewise function given by:

$$P(\phi_1 + \phi_2 + \phi_3) = \frac{4}{\pi^3}(\phi_1 + \phi_2 + \phi_3)^2 \quad (6)$$

over the restricted domain $\phi_1 + \phi_2 + \phi_3 \leq 90^\circ$. For our chondrules, $\phi_1 + \phi_2 + \phi_3 = 44.0^\circ$. Integration of Eq. 6 shows that the probability of mutually random directions resulting in $\phi_1 + \phi_2 + \phi_3 \leq 44.0^\circ$ is 1.9%. We therefore reject the hypothesis that the HC/HT component directions and the chondrule 2D short axes are unrelated at the 98% level, implying that the two directions are mutually aligned. We conclude that HC/HT magnetizations in the dusty olivine-bearing chondrules were likely acquired during spinning and cooling in the solar nebula. Future 3D tomographic imaging combined with paleomagnetic measurements would permit comparison between the magnetization and the true short axis of the chondrule.

3.5. NRM of non-dusty olivine-bearing chondrules. We extracted a total of seven samples from five NDOCs from our Semarkona slices to compare their magnetization to that of dusty olivine-bearing chondrules. Because most non-dusty metal grains in Semarkona have been subject to recrystallization during parent body metamorphism [see Section 2.1; (*19, 66*)], NDOCs are not expected to retain pre-accretional magnetization. We test this hypothesis by performing the same conglomerate test and unidirectionality tests on our NDOC samples.

We subjected all NDOC samples to three-axis AF demagnetization up to 290 mT in steps of 5 mT below 90 mT and in steps of 10 to 50 mT between 90 and 290 mT. We applied AF demagnetization three times at each level ≥85 mT to reduce noise. Furthermore, we averaged the magnetizations of each two adjacent AF steps above 20 mT and each three adjacent steps above 40 mT (see Section 3.3).

Six out of seven NDOC samples carry two components of magnetization while one sample, C4b, carries a single component (Table S3). The NRM components of NDOC samples exhibit a greater diversity of coercivity ranges than dusty olivine-bearing chondrules. Two samples, C2 and C4b, have no stable magnetization above 32.5 mT while C4a loses directional stability by 140 mT. These maximum coercivities are lower than those of dusty olivine-bearing chondrules, suggesting that the main carrier of these magnetizations is mesostasis metal grains, which are much larger than dusty olivine metals and exist in the magnetically soft MD state (*22*). In contrast, the remaining four NDOC samples are not fully demagnetized by 290 mT, possibly due to the presence of fine FeNi grains in the mesostasis.

For the six NDOC samples that carry two magnetization components, the softer LC components of magnetization are blocked between 0 and up to 22.5 mT. In samples C2, C5a, and C4a, this LC component may correspond to the LCa overprint. The HCa magnetizations, so named to avoid confusion with the internally unidirectional HC components found in dusty olivine-bearing chondrules, are found in all NDOC samples and are blocked between the end of the LC component, if one exists, and up to >290 mT. Comparing the values of DANG and MAD (see Section 3.3), only the HCa components found in samples C3, C4a, and C4b are origin-trending, although continued demagnetization of the remaining samples may alter the relative magnitudes of DANG and MAD. The HCa components of magnetization are mutually randomly oriented and pass the conglomerate test at the 95% confidence level (*27*).

Among the five extracted NDOCs, C4 and C5 have been further divided to yield two subsamples each. Unlike dusty olivine-bearing chondrules, subsamples of individual NDOCs have mutually random HCa magnetizations (Fig. NDOC), as the sum of the angular separations between chondrule subsamples is 232°, which corresponds to P value of 0.82 according to Eq. (4). Such internally non-unidirectional magnetization is consistent with acquisition during plessitic exsolution on the LL parent body but inconsistent with a pre-accretional origin (*41, 88*).

We therefore conclude that, as predicted by the petrography of metal phases (Section 2.1), Ni-rich, mesostasis metal grains in Semarkona carry randomly oriented secondary magnetization due to metamorphic recrystallization in a weak field while the Ni-poor dusty olivine metals retain pre-accretional magnetization. The results of these subsampling experiments on both dusty olivine-bearing chondrule and NDOC samples highlight the importance of the unidirectionality test as a complement to the conglomerate test in identifying pre-accretional magnetization. Although the HC/HT/HCa magnetizations in both sets of chondrules pass the conglomerate test, the unidirectionality test supports a pre-accretional origin for only the magnetization in dusty olivine-bearing chondrules.

4. Paleointensities of dusty olivine-bearing chondrules.

4.1. Calculation of paleointensities. As discussed in the main text and Sections 2.1 and 3.3, HC/HT components of dusty olivine-bearing chondrules represent pre-accretional TRMs acquired during cooling in the solar nebula. The paleointensities derived from these components therefore constrain the strength of magnetic fields in the nebular gas, likely during the late cooling stage of chondrule formation.

Experiments on laboratory TRMs imparted on synthetic dusty olivine grains show that the ARM normalization method potentially yields paleointensity estimates accurate to within ~20% (1σ) of the true value for samples whose magnetization is dominated by SV states similar to our dusty olivine-bearing chondrules [see Section 2.2; (*29*)]. The best-fit calibration factor f for such samples is 1.87 [see Eq. (2)]. This ARM calibration is most applicable in the coercivity range 100-150 mT. All HC components found in dusty olivine-bearing chondrules are blocked across this coercivity range. Furthermore, the ratio of ARM to NRM loss does not show significant variation across the coercivity range of the HC component (Fig. S11). We therefore use the

ARM calibration inferred from the 100-150 mT range to calculate the paleointensity for the full HC component. Finally, our applied bias field of 100 μT for the ARM acquisition experiments is well within the range where ARM intensity varies linearly with the bias field. For these reasons, we expect similar performance of the ARM normalization method for our dusty olivine-bearing chondrules compared to the SV grains dominated synthetic dusty olivine grains used by Lappe et al. (*29*), implying that 1σ uncertainty due to the ARM calibration factor is ~20%.

Due to its well determined calibration, we use the ARM normalization method to infer paleointensities for all dusty olivine-bearing chondrule samples that carry an HC component except DOC4S (see below). We first imparted an ARM with an AC field of 290 mT and a bias field of 100 μT. We then subjected the ARM to AF demagnetization using the same sequence of steps as during AF demagnetization of the NRM for each sample. Finally, we averaged multiple measurements at the same AF level and across adjacent AF levels as was done for the NRM.

To derive paleointensities, we then compared the vector change in NRM with that of ARM for AF levels in each component and used a linear least-squares fit to obtain the ratio $\Delta NRM/\Delta ARM$ (Fig. S11). We then applied Eq. (2) and corrected the resulting raw paleointensities for effect of sample anisotropy [e.g., (*93*)], which may be a significant effect for samples whose HC component direction was offset from that of the ARM bias field (Table S4). For DOC3 and DOC4, we averaged the paleointensities derived from each subsample to obtain the representative paleointensity for the whole chondrule. In the case of DOC4S, the coercivity range of the HC component extends to 420 mT, which is above the maximum AC field level available for an ARM. We therefore use the IRM normalization method for this sample by imparting a 400 mT IRM followed by stepwise demagnetization up to 420 mT. Similar to our ARM normalization procedure, we ratio the vector change in NRM and IRM for each component and calculate the paleointensity using Eq. (1). To derive the IRM calibration factor a, we performed an identical IRM paleointensity experiment on the subsample DOC4N, which originates from the same chondrule and for which we also have ARM normalized paleointensities. Assuming that the IRM normalized paleointensity for DOC4N equals the ARM normalized value, we find that a=3100 μT, which is similar to typical values for iron-bearing lunar samples (*80*).

We consider two sources of uncertainty in the paleointensity of each dusty olivine-bearing chondrule. First, the linear fit to determine the ratio $\Delta NRM/\Delta ARM$ or $\Delta NRM/\Delta IRM$ carries uncertainties of typically 20-30% (1σ). Second, the ARM calibration factor, where used, is subject to uncertainty of ~20% (see above). We assume that the two sources of errors are independent for each chondrule. Further, we assume that the uncertainties in ARM calibration factor for each subsample of DOC3 and DOC4 are also mutually independent. Total 1σ uncertainties in the ARM and IRM normalized paleointensity of each chondrule derived from the combination of these two sources range between 26% and 50% (Table S4).

One final source of uncertainty arises due to the rotation of chondrules during remanence acquisition (see Section 3.4). Tomographic studies of chondrule morphology imply that, above the solidus [~1000˚C; (*104*)], chondrules rotated with angular velocities 50-350 s^{-1} around the chondrules' symmetry axis (*30, 99*). Upon cooling across the solidus, chondrules would have retained rotation around the same spin axis unless perturbed by external torques, which may have led to precession of the spin axis.

We first address the correction to the measured paleointensity assuming that negligible precession occurs and the chondrule maintains spin around its axis of highest moment of inertia. The magnetic field intensity recorded by a spinning chondrule (B_{rec}) is the projection of the true ambient field (B_{amb}) onto the chondrule spin axis. Assuming that the orientation of the spin axis is independent of the local magnetic field, the probability distribution function of B_{rec} is a simple uniform distribution [(*105*), p. 30]:

$$P(B_{rec}) = \frac{1}{B_{amb}}. \tag{7}$$

over the domain $0 \leq B_{rec} \leq B_{amb}$. Given a finite number of measurements, the probability density distribution of the mean of the chondrule paleointensities ($\overline{B}_{rec}$) may be found by the repeated convolution of Eq. (7) with itself. By the central limit theorem, the probability distribution function of $\overline{B}_{rec}$ approaches a Gaussian distribution centered on $\frac{1}{2}B_{amb}$ [(*105*), p. 252]. For a sample size of five, we find that the probability distribution function of $\overline{B}_{rec}$ very closely approximates a Gaussian distribution with standard deviation $0.13B_{amb}$. In summary, for the non-precessing case, the best guess ambient field strength is twice our mean paleointensity while the additional 1σ uncertainty due to rotation and our finite sample size is 0.13 of the true field. Applying this, we find a true ambient field strength of 54±21 μT (2σ).

We now address the correction to the paleointensity assuming that precession of the chondrule was significant. If the uniform rotation of the chondrule is disturbed after cooling below the solidus, the elastic nature of the solid chondrule implies that the damping timescale of precession is much longer than the cooling timescale of chondrules [(*106*), p. 92], implying that once a chondrule is precessing, it would continue to do so over the course of remanence acquisition. The precession rate of the instantaneous rotation axis in the body frame of the chondrule is a function of its oblateness and rotation rate [(*107*), pp. 396-399]. For a chondrule with an aspect ratio ~1.3 (e.g., DOC4; Figs. 1A and S10C) spinning at 140 s^{-1} (*30*), the precession frequency is 36 s^{-1}, implying that precession occurs on much shorter timescales than that of chondrule cooling. Azimuthal (i.e., perpendicular to the chondrule's symmetry axis) components of remanence therefore average to zero during remanence acquisition. The magnetization acquired by a precessing chondrule is then parallel to the symmetry axis, which is consistent with the observed alignment between HC direction and chondrule short axes, although this alignment is also consistent with non-precessing rotation.

We therefore calculate the expected intensity of magnetization acquired in an ambient field B_{amb} by finding the time-averaged projection of $\vec{B}_{amb}$ onto the chondrule symmetry axis. We adopt a fixed frame where the angular momentum vector ($\vec{L}$) is aligned with the positive z axis, $\vec{B}_{amb}$ is offset from $\vec{L}$ by angle θ_B, and the symmetry axis ($\hat{c}$) of the chondrule is offset from $\vec{L}$ by angle θ_c. Due to its precession around $\vec{L}$, $\hat{c}$ is given by $(\sin\theta_c \cos\omega_p t,\ \sin\theta_c \sin\omega_p t,\ \cos\theta_c)$, where ω_p is the precession frequency [(*107*); pp. 396-399]. Assuming no significant external torques, $\vec{B}_{amb}$ is constant in this reference frame and can be denoted by $B_{amb}(\sin\theta_B,\ 0,\ \cos\theta_B)$. The time average of the dot product $\vec{B}_{amb} \cdot \hat{c}$ is then given by:

$$\vec{B}_{amb} \cdot \hat{c} = B_{amb} \cos\theta_B \cos\theta_c. \tag{8}$$

Assuming that the orientation of $\vec{L}$ is independent of $\vec{B}_{amb}$, the expectation value of the recorded paleointensity ($\overline{B}_{rec}$) can be found by integrating Eq. (7) weighted with the probability distribution function of θ_B, which is $P(\theta_B) = \sin\theta_B$ on the relevant domain $0 \le \theta_B \le \pi/2$. We then arrive at the equation:

$$\overline{B}_{rec} = 1/2 B_{amb} \cos\theta_c, \tag{9}$$

which is identical to the non-precessing case except for the factor $\cos\theta_c$. For weak precession (i.e., $\theta_c \approx 0$), we recover the previous relationship $\overline{B}_{rec} = 1/2 B_{amb}$. If we assume that θ_c is randomly distributed (i.e., strong precession, implying frequent processes that disturb the rotational axis of the chondrule from the original non-precessing direction), the expectation value of $\overline{B}_{rec}$, found by again integrating Eq. (9) weighted by $P(\theta_c)$, yields the relationship $\overline{B}_{rec} = 1/4B_{amb}$, implying a maximum true ambient field intensity 4 times our measured paleointensity.

However, we argue that the amplitude of precession was likely small in chondrules (i.e., $\theta_c \approx 0$), which would imply that $\overline{B}_{rec} \approx 1/2B_{amb}$ as in the non-precessing case. To impart significant precession to a chondrule, external processes must contribute angular velocities not negligible compared to the 50-350 s^{-1} values for chondrules within the several hour timespan of chondrule cooling.

Collisions with gas molecules may perturb the original spin axis of the chondrule. The contribution to the angular momentum of the chondrule from a single gas molecule collision is $dL \approx mvr_c$ where m is the mass of the gas molecule, v is its velocity, and r_c is the chondrule radius. Because the gas molecules arrive from random directions, the total contribution to the angular momentum can be described by a random walk and is given by $\Delta L \approx \sqrt{N}dL$ [(*108*); p. 34], where $N = 4\pi v n r_c^2 t$ is the number of collisions in time t and in a gas with number density n. Approximating a chondrule as a uniform sphere with 0.6 mm diameter and assuming a gas environment with v = 3000 m s^{-1} and $n = 1.8\times10^{21}$ m^{-3} (*10*), the associated angular velocity acquired in one hour is only ~0.01 s^{-1}, which is negligible compared to the original chondrule angular velocity.

We next consider collisions with dust particles as the source of external torque. Assuming collision velocities of 1 m s^{-1} between chondrules and 1 μm dust grains and a dust to gas ratio of 0.01 (*109*), we find that 2500 collisions occur in each hour, imparting an angular velocity of ~0.02 s^{-1}.

Finally, we consider collisions with other chondrules. Such collisions can impart large angular velocities to chondrules (*110*). The frequency of compound chondrules is 5%, which represents a lower bound to the frequency of collisions during cooling between approximately 1500 and 1100˚C (*109, 111*). Assuming that the rate of cooling did not change at the lower temperatures relevant to remanence acquisition, this implies that few chondrules should have been affected by such collisions. In summary, precession can lead to a discrepancy of up to a factor of 4 between B_{amb} and our measured mean paleointensity while rotation around a single spin axis would imply a factor of 2. We find that known processes are unlikely to have induced significant precession of chondrules within the cooling timescale. We therefore regard rotation around a single spin axis as the most likely state of motion for a cooling chondrule, leading to a discrepancy factor of 2 and an inferred ambient field strength of 54±21 μT (2σ).

5. Comparison with theoretically predicted field strength.

5.1. General considerations. Magnetic mechanisms are a promising solution to the problem of rapid gas accretion in the solar nebula and other protoplanetary disks (*5*), which have typical observed accretion rates between 10^{-9} and 10^{-7} M_{Sun} y^{-1} where M_{Sun} is the sun's mass (*2, 112*). In this section we summarize the relationship between magnetic field strength and mass accretion rate, thereby deriving the accretion rate given our experimental nebular paleointensities. We then compare these inferred accretion rates with observational constraints.

Accretion disk magnetic fields may transport angular momentum in two fundamental ways. The first is to transport angular momentum radially outward by the $R\phi$ component of the Maxwell stress tensor, given by $T_{R\phi}=-B_R B_\phi/4\pi$, where R and ϕ are the radial and azimuthal coordinates, respectively. This can be achieved either from turbulent magnetic fields, most plausibly from the MRI (*113, 114*) or contributions from the large-scale field via magnetic braking, especially when the disk is threaded by external magnetic flux (*115-117*). Assuming the $R\phi$ Maxwell stress is exerted through a layer with thickness comparable to the disk scale height $H=c_s/\Omega$, where c_s is the isothermal sound speed [given by $(kT/\mu m_{\mathrm{H}})^{1/2}$ where k is the Boltzmann constant, T is the local disk temperature, m_{H} is the mass of hydrogen, and μ=2.34 describes the mean particle mass of the nebular gas] and Ω is the local angular velocity, the steady-state accretion rate is given by (*3, 4*):

$$\dot{M} \approx \frac{|B_R B_\phi| H}{2\Omega}. \tag{10}$$

Since $B^2 \geq B_R^2+B_\phi^2 \geq 2|B_R B_\phi|$, the above equation yields a lower limit on the total magnetic field strength at a given accretion rate, which can be expressed as [see ref. (*4*) for complete derivation]:

$$B \geq 1.0\times10^2\, \dot{M}_{-8}^{1/2}\, R_{AU}^{-11/8}\ \mu\mathrm{T}, \tag{11}$$

where R_{AU} is the disk radius is AU, $\dot{M}_{-8}$ is the accretion rate normalized to 10^{-8} M_{Sun} y^{-1}, and we have assumed that $T = 280\ R_{AU}^{-1/2}$ K (*59*).

The second way is to transport angular momentum vertically and outward via the $z\phi$ component of the Maxwell stress tensor, given by $T_{z\phi}$=-$B_z B_\phi/4\pi$. This can be achieved by the magnetocentrifugal wind (*118*). Accretion is driven by the torque $RT_{z\phi}$ exerted at the disk surface, which leads to an accretion rate (*3, 4*):

$$\dot{M} \approx \frac{2\left|B_z B_\phi\right| R}{\Omega}. \tag{12}$$

Similarly, a lower limit on the total magnetic field strength in this scenario can be estimated to be [see ref. (*4*) for complete derivation]:

$$B \geq 10\, \dot{M}_{-8}^{1/2}\ R_{AU}^{-5/4}\ \mu\text{T}, \tag{13}$$

which is largely independent of assumptions about disk model. We see that given similar level of stress, disk wind is more effective in driving accretion than the radial transport of angular momentum by a factor of R/H ~ 30 in the inner disk. Therefore, the disk wind requires weaker magnetic fields to achieve a given accretion rate.

Comparing these results with the inferred our experimental paleointensities (Fig. S12), we see that for a typical accretion rate of 10^{-8} M_{Sun} y^{-1} at the expected radius of R~2.5 AU, radial transport of angular momentum via the MRI or magnetic braking is possible if the disk magnetic field is ≥30 μT. In the case of wind-driven accretion, any disk field strength ≥3 μT would drive accretion at >10^{-8} M_{Sun} y^{-1}. Given our recovered paleofield intensity during chondrule formation of 54±11 μT, the MRI or magnetic braking would drive sufficient mass accretion in the solar nebula if background fields were amplified by less than a factor of ~2 during chondrule formation. For wind-driven accretion, even field amplification of 10× during chondrule formation, which is the highest amplification factor expected in the nebular shock (*10*), would imply sufficient background magnetic fields strength to drive disk accretion. Therefore, regardless of the type of chondrule formation mechanism, our experimental magnetic fields imply that magnetic mechanisms can readily account for the bulk of mass and angular momentum transport in the solar nebula.

5.2. Comparison with recent simulations. One uncertainty about the general discussion above is that our sample most likely records the magnetic field near disk midplane, while the lower limit of magnetic field strength in the two scenarios (11) and (13) only applies to regions where the $R\phi$ and $z\phi$ Maxwell stress is exerted. In particular, the wind stress $T_{z\phi}$ is exerted at the disk surface, which does not necessarily have the same field strength as that at the midplane. Therefore, comparison with detailed models of protoplanetary disks is necessary.

The gas dynamics and magnetic field structure in protoplanetary disks/solar nebula are strongly controlled by non-ideal magnetohydrodynamic effects including Ohmic resistivity, Hall effect and ambipolar diffusion (*5*). While the effect of Ohmic resistivity has been studied for over a decade (*119*), systematic exploration of ambipolar diffusion and the Hall effect began only recently. It has been found in simulations that, in the inner region of protoplanetary disks up to 10 AU, the MRI is suppressed and accretion is instead driven by the magnetocentrifugal wind (*115, 120*). Inclusion of the Hall effect makes gas dynamics and magnetic field structure depend on the polarity of the net vertical magnetic field with respect to the angular momentum vector (rotation axis) of the disk. This polarity leads to markedly different behaviors especially in the inner disk (*116, 117, 121, 122*).

Full discussion about these effects is beyond the scope of this paper, and there remain several unresolved issues particularly concerning the wind geometry and kinematics. In brief, when the external vertical field is aligned with disk rotation, we expect amplification of the R and ϕ magnetic field components around disk midplane due to the Hall-shear instability (*123*). In this case, estimates based on Eq. (11) are relatively reliable if magnetic braking is the only mechanism operating. For the wind scenario, Eq. (13) is likely an underestimate since the midplane field can be much stronger than the surface field [but still lower than that in equation (9)]. When the external vertical field is anti-aligned with disk rotation, current simulation results suggest wind-driven accretion with stress exerted at the disk surface, while the midplane field is mostly vertical whose strength is of the order 1 μT for typical accretion rates, which are too weak to be consistent with our experimental results. Therefore, our results may further suggest that the solar system was formed with its large-scale poloidal magnetic field aligned with disk rotation.

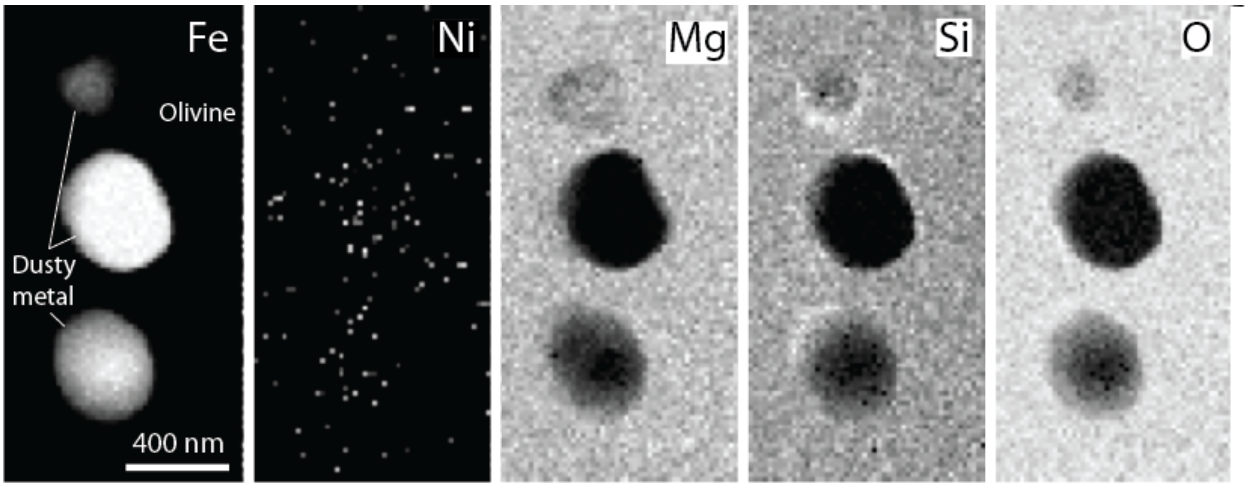

Figure S1. STEM elemental maps of three dusty metal grains in the chondrule DOC5. Note the absence of Ni and the forsteritic composition of the surrounding olivine.

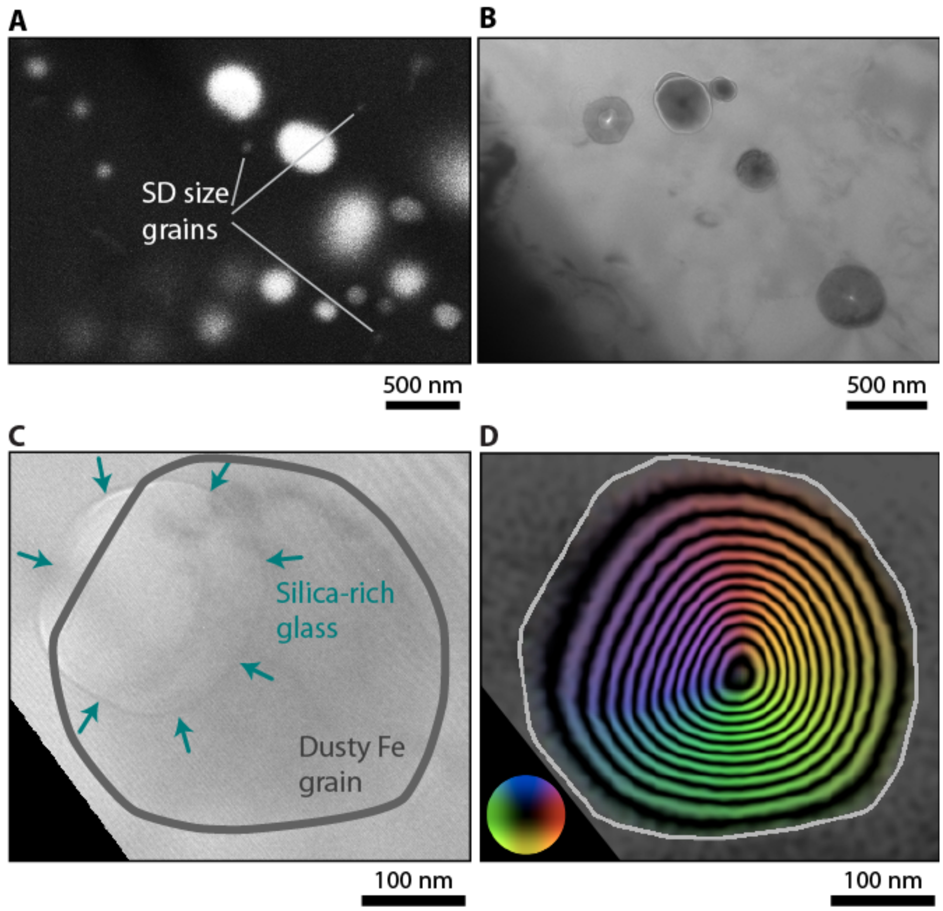

Figure S2. High resolution microscopy and electron holography of dusty olivine metals. (**A**) Secondary electron image of dusty olivine metals in chondrule sample DOC4S. Metal grains with size of ~60 nm are likely in the SD state, while the remaining grains are in the SV state. Unsharp grain boundaries in part (A) indicate that the metal grain is not exposed at the sample surface. Grain sizes were determined by integrating the intensity at all azimuths for each radius from the grain center and finding the radius at which the integrated intensity falls to 50% of the interior value. This procedure provides an averaged diameter for non-circular grains and has an uncertainty of ~10 nm in diameter. (**B**) Lorentz image of dusty olivine metals in chondrule DOC5. Particles exhibit a dark or bright spot contrast around the core, suggesting the SV state with different magnetization directions (*124*). (**C**) Electron hologram of a single dusty olivine Fe grain and associated silica-rich glass in chondrule DOC5 and (**D**) magnetic induction map of the same field of view, showing the azimuthal magnetization expected of a grain in the SV state with vortex core pointing out of the plane. The image in part (A) was obtained using a Zeiss NVision40 SEM with a 15 keV beam at 5.0 mm working distance at the Harvard University Center for Nanoscale Systems. The Lorentz image and the electron hologram in parts (B-D) were obtained with an FEI Titan 300 keV TEM at the Center for Electron Nanoscopy.

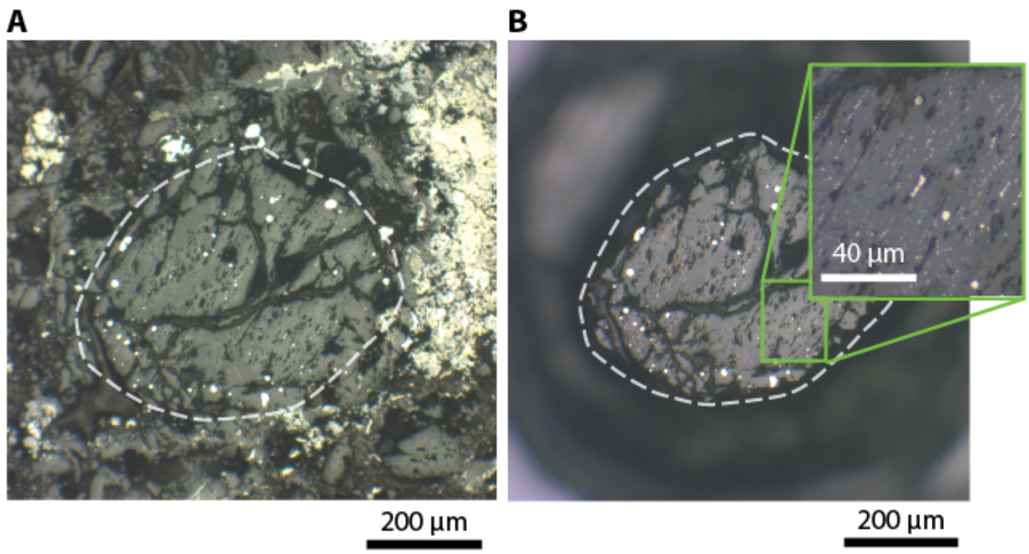

Figure S3. Reflected light photomicrographs showing the extraction procedure applied to dusty olivine-bearing chondrule DOC1. The in-section chondrule (**A**) is isolated by the removal of surrounding rim and matrix material using a micromill. The isolated chondrule (**B**) is then magnetically mapped using the SQUID microscope. Inset in part (B) shows a close up reflected light image of dusty olivine metals (white points).

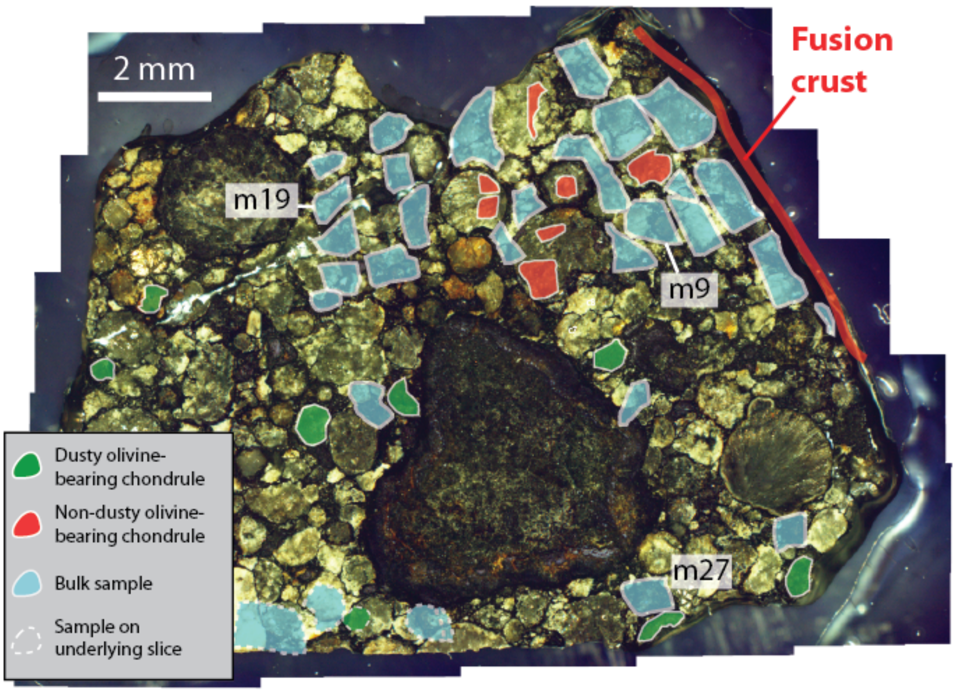

Figure S4. (**A**) Optical image of the ps8 slice of the Semarkona meteorite showing locations of all samples used in this study. Highlighted regions with dashed outline denote the approximate locations of samples extracted from the ps3 slice, which lies 0.9 mm beneath ps8. The AF demagnetization sequences of samples labeled m9, m19, and m27 are shown in Fig. S5.

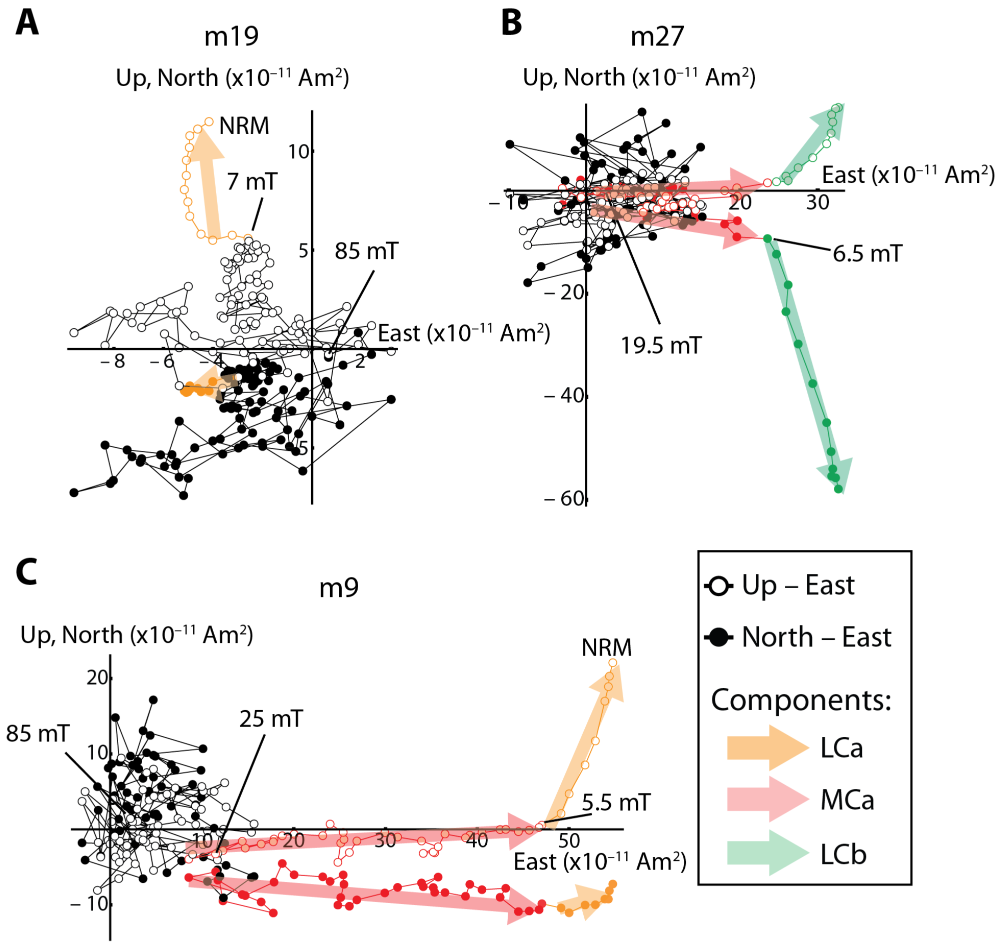

Figure S5. Demagnetization sequences of representative bulk samples showing all three post-accretional overprints. Orthogonal vector endpoint diagrams show the evolution of the NRM vector during AF demagnetization up to 85 mT. Open and closed circles indicate the projection of the magnetization vector onto the vertical (up-east) and horizontal (north-east) planes, respectively. Relative positions of the three samples in the parent Semarkona piece are shown in Fig. S4.

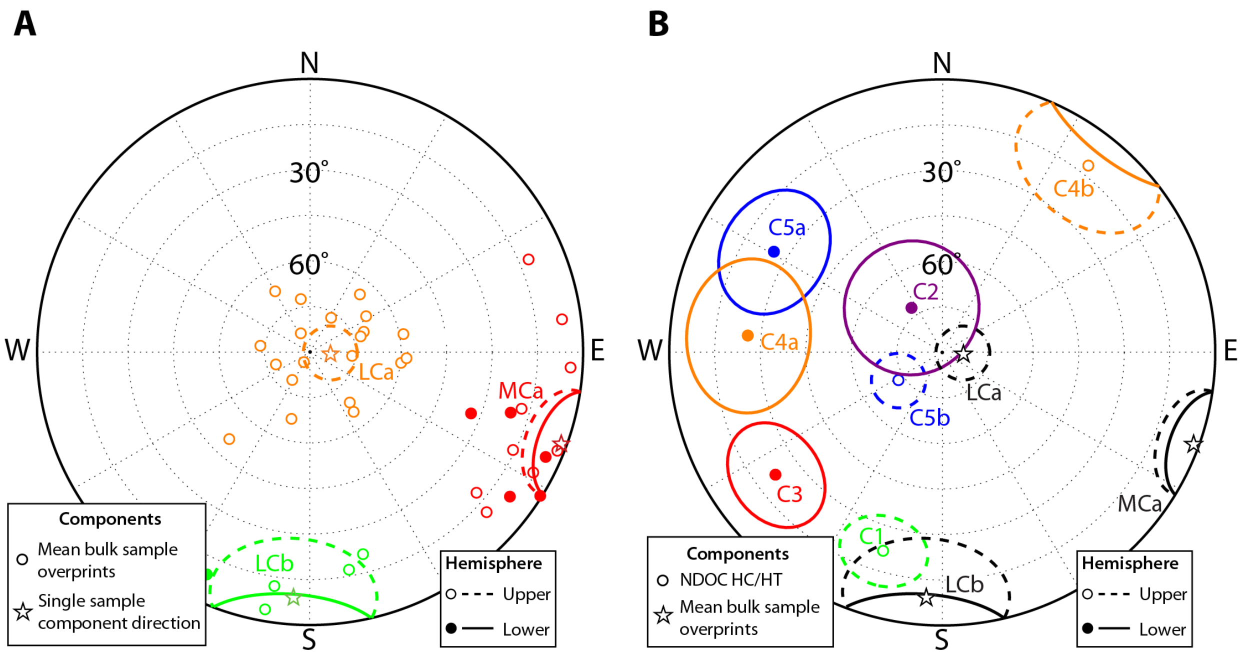

Figure S6. Equal area stereonet projections of (**A**) overprint directions in bulk samples and (**B**) highest coercivity directions in NDOC samples. Open (closed) circles denote PCA-fitted directions of components from single samples in the upper (lower) hemispheres while stars represent the mean directions derived from a group of samples. Ovals around circles and stars indicate the MAD and the 95% confidence interval for the true component direction, respectively.

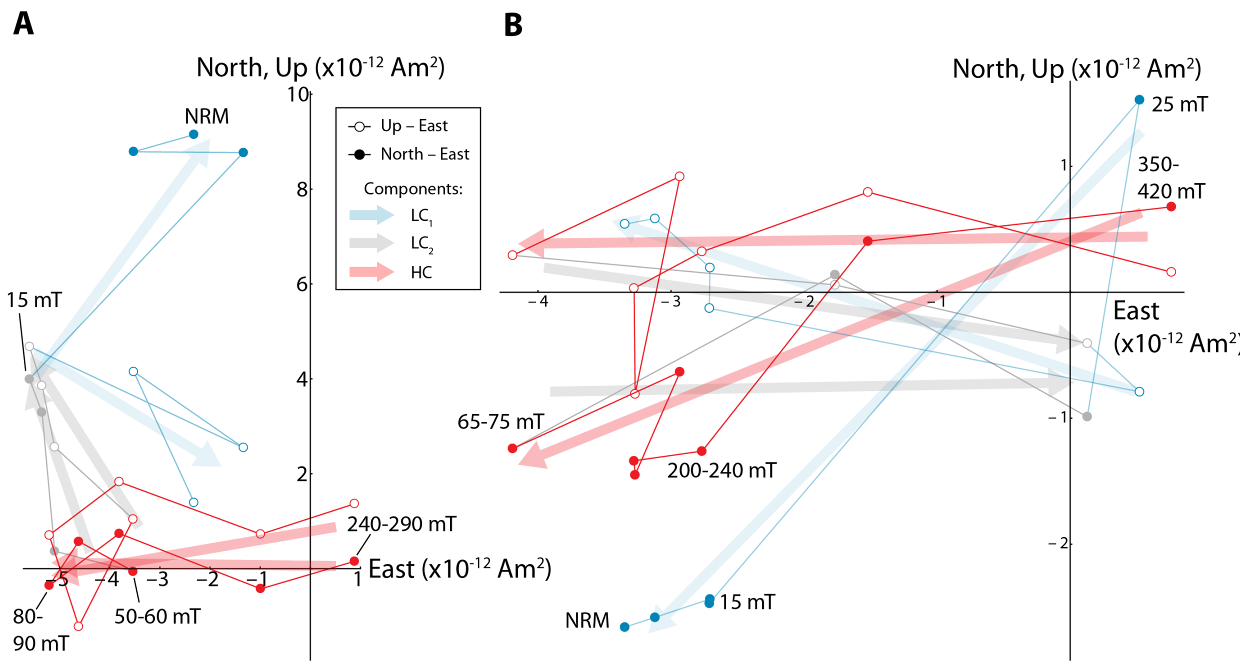

Figure S7. Demagnetization of subsamples of the dusty olivine-bearing chondrule (**A**) DOC4N and (**B**) DOC4S. Orthogonal vector endpoint diagrams show the evolution of the NRM vector during AF demagnetization. Open and closed circles indicate the projection of the magnetization vector onto the vertical (up-east) and horizontal (north-east) planes, respectively. We attribute the non-unidirectional LC components to spontaneous magnetizations acquired during metamorphic recrystallization. In contrast, the unidirectionality of the HC components suggests a TRM origin (see Sections 3.3-3.4).

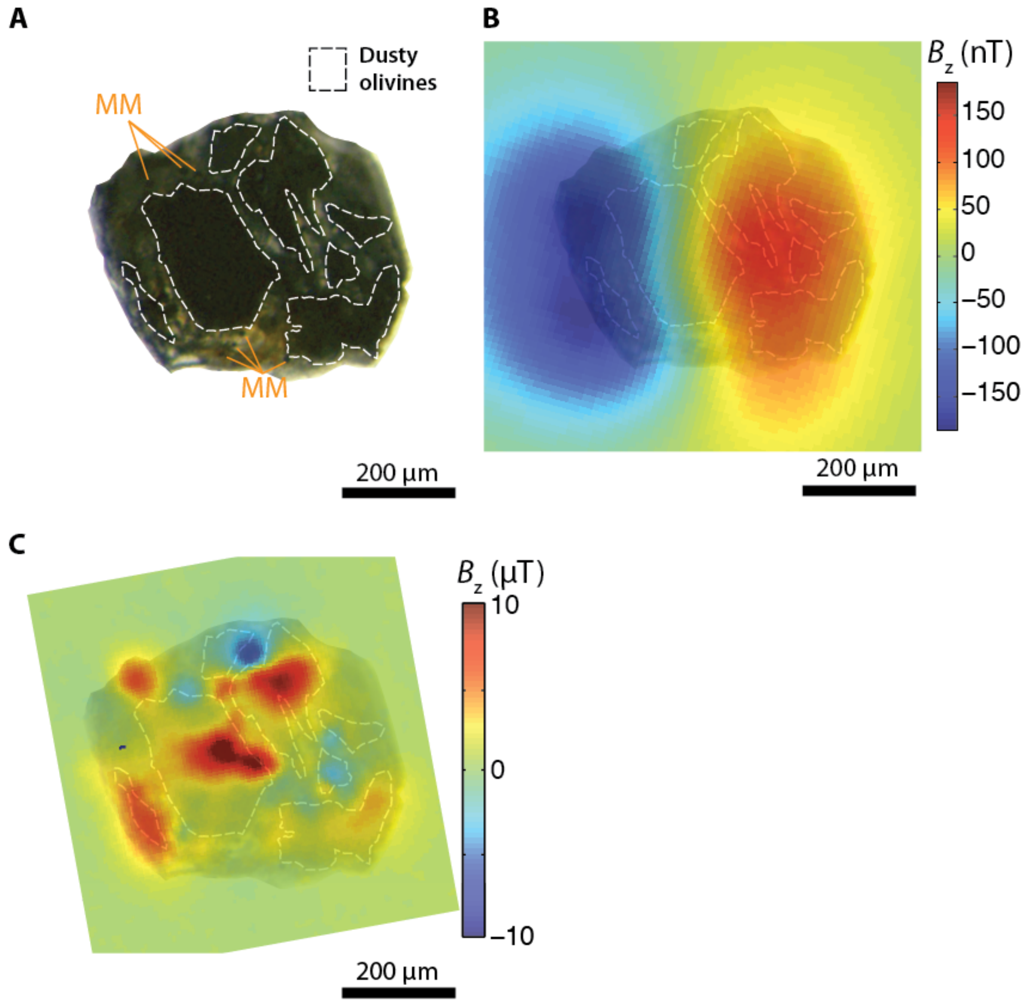

Figure S8. (**A**) Transmitted light optical photomicrograph of sample DOC1, (**B**) overlay of the magnetic field map of the NRM upon AF demagnetization to 50 mT and the optical image in part (A), and (**C**) overlay of the magnetic field map of an AF cleaned laboratory ARM and the optical image in part (A). In both magnetic maps, positive B_z corresponds to the out of the page direction. White dashed outlines in part (A) denote the location of dusty olivine grains, which are optically opaque. Orange line segments point to mesostasis metal grains (MM). Magnetic fields generated by the NRM shown in part (B) were mapped with the MIT SQUID Microscope. Laboratory ARM in part (C), which was mapped using an NV quantum diamond magnetometer, consists of a 290 mT AC field with a 600 μT bias field that was AF demagnetized to 100 mT to simulate part of the coercivity range of the HC component. The ARM bias field was applied in the positive z direction, implying that locations with strong positive B_z correspond to those of magnetic remanence carriers. Note the spatial correspondence between the largest concentration of dusty olivines in part (A), the center of the dipolar source in part (B), and the strongest magnetic sources in part (C).

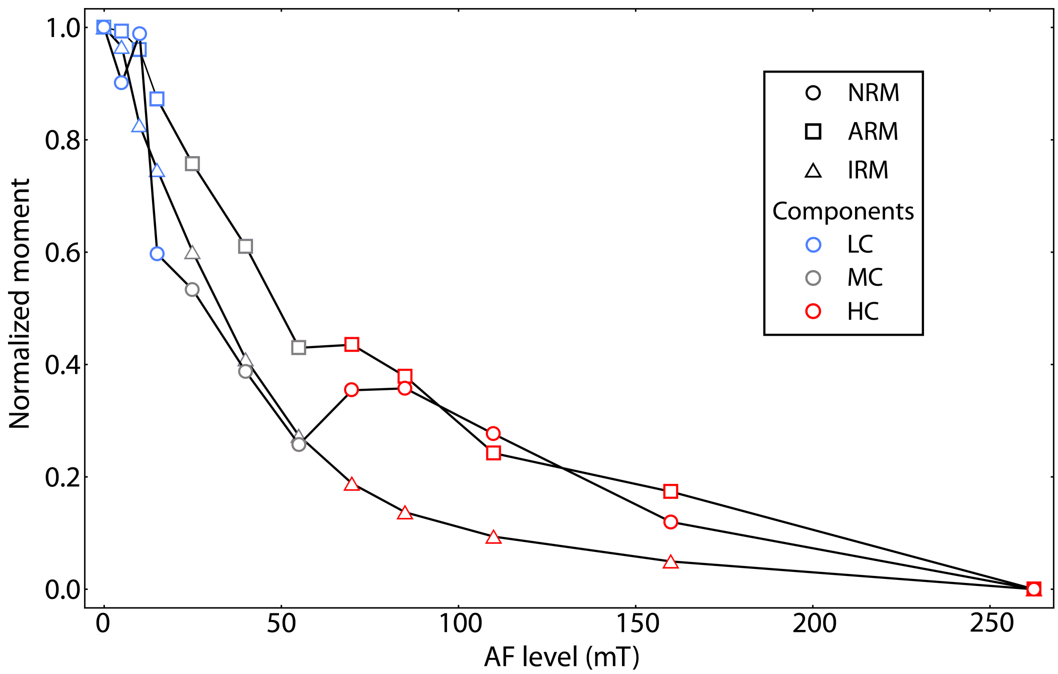

Figure S9. Comparison of the coercivity spectrum of an NRM, ARM, and IRM between 0 and 262.5 mT for dusty olivine-bearing chondrule sample DOC4N. The NRM coercivity spectrum in the HC component range is more similar to the ARM (AC field 290 mT; bias field 100 μT) than the 420 mT IRM, suggesting a TRM origin for the HC magnetization. For the NRM, we corrected for the non-parallel directions of the LC, MC, and HC components by computing the moment at a given AF level using the vector difference with the moment at the highest AF level of the corresponding component.

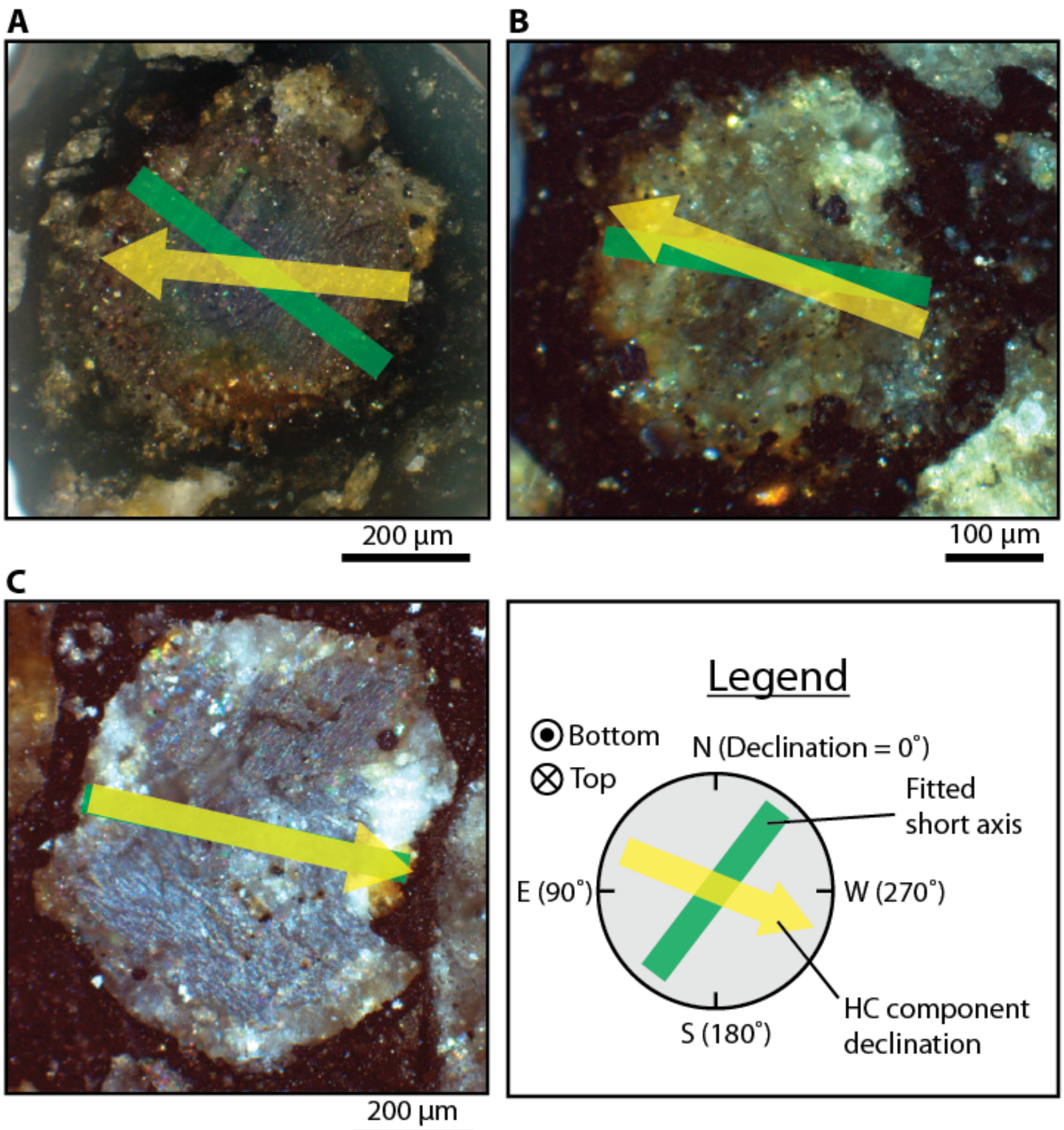

Figure S10. Reflected light photomicrographs of dusty olivine-bearing chondrule (**A**) DOC1, (**B**) DOC2, and (**C**) DOC4 showing the correspondence between the physical short axis and the horizontal projection of the HC magnetization. To obtain the best-fit ellipses and the short axis orientation, we used images of the bottom side of the sample slice due to the availability of higher quality photographs. Note the resulting reversed (counter-clockwise) sense of the declination scale.

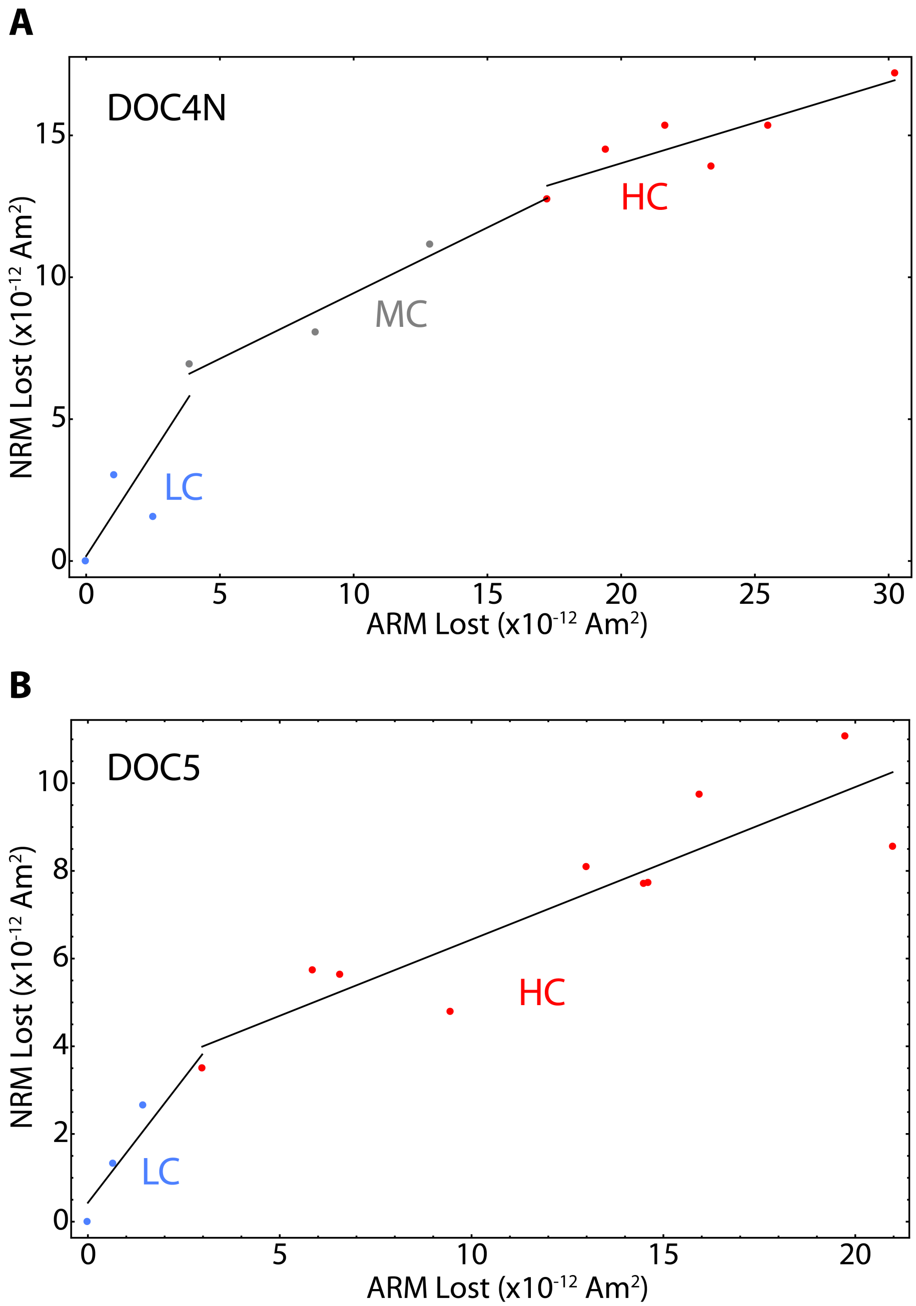

Figure S11. Representative ARM paleointensity experiments on dusty olivine-bearing chondrule samples (**A**) DOC4N and (**B**) DOC5. Data points belonging to each component follow the same color-coding convention as Figs. 2, S7, and S9.

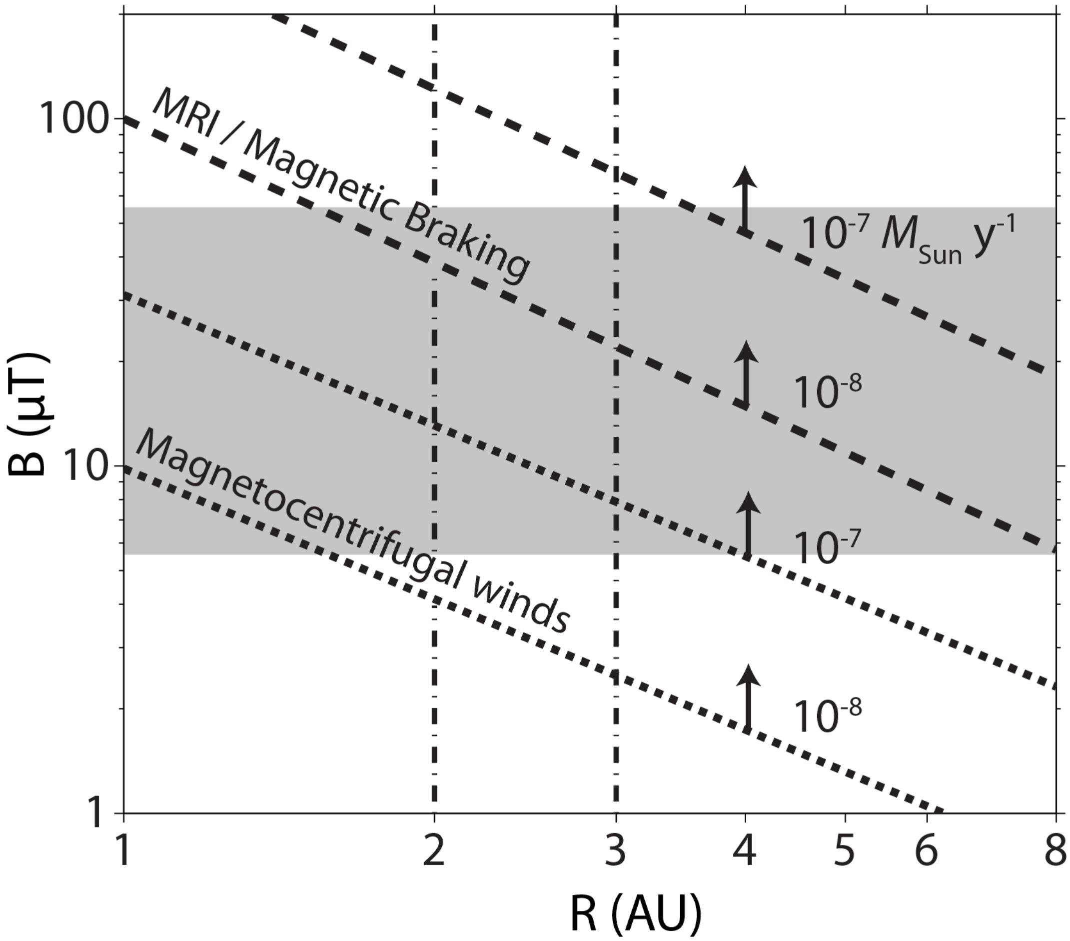

Figure S12. The minimum magnetic field strength as a function of disk radius at a given accretion rate. Dashed and dotted lines correspond to accretion driven by radial transport of angular momentum (due to MRI or magnetic braking) and by vertical transport of angular momentum (due to magnetized disk wind), respectively. The range of background disk magnetic field strength from our experimental results is denoted in gray (5-54 μT). The 2-3 AU region between the dot-dashed lines represent the probable source region of Semarkona based on the distribution of S-type asteroids, which are associated with ordinary chondrites such as Semarkona (*8, 33*). Note that dashed and dotted lines represent lower bounds for the magnetic field strength expected for a given mechanism, orbital radius, and accretion rate.

Table S1: Summary of paleomagnetic results from dusty olivine-bearing chondrules

Sample	Mass (mg)	NRM moment (10^{-4} A m^2 kg^{-1})	Compo-nent	AF or temperature range (mT or °C)	*N*	Dec, Inc (°)	MAD/ α_{95} (°)	DANG (°)	Anisotropy-corrected Dec, Inc (°)
DOC1	0.066	15	LC	0-20	5	297.3, 46.7	10.1		
			HC	20->360	12	84.6, 28.0	10.9	9.4	89.4, 18.4
DOC2	0.027	6.6	LC	0-87.5	11	273.0, 50.6	20.8		
			HC	85-290	6	69.4, -46.4	16.8	1.5	50.5, -38.4
DOC3N	0.0027	3.6	LC	0-20	5	110.0, -65.0	27.0		
			HC	20-290	13	338.8, 76.9	17.8	11.3	3.6, 79.2
DOC3S	0.0094	3.7	LC	0-10	4	330.1, -41.2	7.6		
			HC	10-290	14	110.7,66.1	27.8	11.2	96.5, 59.4
DOC4N	0.019	5.0	LC_1	0-15	4	36.3, 23.0	19.8		
			LC_2	15-55	4	337.8, -35.9	13.1		
			HC	50-290	6	272.3, -6.7	18.6	18.0	264.2, -13.3
DOC4S	0.014	3.1	LC_1	0-40	6	226.3, -12.2	13.3		
			LC_2	40-70	3	84.9, 9.0	18.1		
			HC	65-420	7	251.1, -2.8	13.0	7.4	246.9, -6.8
DOC5	0.085	0.35	LCb	0-15	4	205.9, 4.9	27.3		
			HC	15-290	10	18.1, -1.8	21.4	19.0	25.6, -6.1
DOC6	0.030	9.5	LC	0-50	11	301.2, 25.6	34.9		
			MCa	50-120	5	124.6, -3.7	16.1		
DOC7	0.039	0.18	LC	0-30	7	20.3, 2.3	15.6		
DOC8	0.0077	3.2	LCb	0-22.5	7	179.2, -31.0	24.3		
			HT	350-750	8	80.2, 61.3	17.6	13.3	N/A
LCa					20	92.4, -83.3	8.9		
MCa					14	109.9, -2.0	11.7		
LCb					5	183.9, -9.2	19.2		

Note: All samples in table are mutually oriented to within ~5°. All samples were subjected to AF demagnetization except DOC8, which was subjected to thermal demagnetization after AF cleaning to 22.5 mT. For comparison, the mean direction and 95% confidence interval of the three post-accretional overprints are given at the end of the table. The first column gives the sample name; the second column give the mass; the third column gives the mass-normalized NRM moment; the fourth column gives the component name; the fifth column gives the coercivity or temperature range of the component; the sixth column gives the number of AF or thermal steps in each component or the number of samples in a mean direction; the seventh column gives the direction of the component as calculated from PCA or mean direction; the eighth column gives the maximum angular deviation (MAD) of the component or the 95% confidence interval (α_{95}) of the mean direction (see Section 3.3); the ninth column gives the deviation angle (DANG); the tenth column gives the component direction as given in column seven after correction for anisotropy, which is based on the measured anisotropy of ARM of each sample.

Table S2: Summary of paleomagnetic results from bulk samples.

Sample	Mass (mg)	NRM moment (10^{-4} A m^2 kg^{-1})	Distance to fusion crust (mm)	Demagnet-ization Method	Compo-nent	AF or temperature range (mT or °C)	*N*	Dec, Inc (°)	Paleointensity (μT; IRM, ARM)
m1	0.59	8.0	0.0	AF	LCa	0-8	15	96.9, -59.7	
					MCa	8-20	25	122, 0.3	
					U	24.5-85	62	220.2, 34.7	
m2	0.30	32	0.0	AF	LCa	0-8	15	222.5, -50.9	12, 95
					MCa	8-22	29	110.8, 33	22, 76
					U	22-40	22	160.7, -5	18, 60
					U	40-85	46	66.5, 50.2	22, 20
m3	0.40	13	0.9	AF	LCa	0-9	17	141.4, -68.6	12, 161
					U	9-26	34	303.9, 0.2	4, 34
m4	0.42	14	0.8	AF	U	0-7	13	348.5,4.6	66, 458
					U	8-85	97	159.7, -22.3	3, 19
m5	0.08	18	0.8	AF	LCa	0-8	15	93.9, -57.9	
					MCa	8-19	23	67.1, -11.7	
					U	19-29	17	50, 43.1	
m6	0.41	9.5	1.9	Thermal	LTa	20-70	23	57.7, -68	
					MTa	70-220	15	114, 4.7	
m7	0.40	3.3	0.8	AF	LCa	0-6	11	276.6, -73.8	
					MCa	6-31	45	106.9, 20.8	
m8	0.36	17	1.4	AF	LCa	0-5	9	69.8, -71	
					MCa	5-230	37	93.4, -3.9	
m9	0.05	120	0.0	AF	U	4-26	44	59.2, 62.2	
m10	0.27	10	2.8	AF	LCa	0-6	11	143.6, -65.3	17, 278
					MCa	6-12.5	14	115.7, -15.5	16, 120
m11	0.16	21	3.0	AF	LCa	0-8.5	16	143.6, -65.3	
					MCa	8.5-23	30	130.3, -18	
m12	0.18	25	2.0	AF	LCa	0-4.5	8	73.5, -72.4	
					MCa	4.5-8	8	105, -17.5	
m13	0.24	11	4.1	AF	LCa	0-11.5	22	32, -76.7	12, 92
					MCa	11.5-28	31	125.8, 8.5	7,33
m14	0.34	8.4	4.7	AF	LCa	0-5	9	95.2, -75.8	26, 220
					MCa	5-7.5	6	132.1, -11.2	15, 216
m15	0.21	10	4.9	AF	LCa	0-8.5	16	79.3, -58.4	32, 145
m16	0.16	18	4.3	AF	LCa	0-4.5	8	330.4, -67	
m17	0.21	2.8	6.3	AF	LCa	0-7	13	333.8, -83.2	
m18	0.20	6.2	5.7	AF	LCa	0-7	13	249.2, -78.1	
m19	0.22	18	5.8	AF	LCa	0-6.5	12	350.8, -72.4	
m20	0.09	3.5	5.7	AF	LCa	0-6	13	194.9, -67.1	
m21	0.36	5.0	7.6	AF	LCa	0-7.5	14	211.2, -79.1	
m22	0.18	16	3.4	AF	LCa	0-5.5	10	41.5, -64.9	25, 195
					MCa	5.5-28	43	82.7, -6.2	8, 27
m23	0.19	71	1.7	AF	MCa	0-21	41	118.4, -6.3	57, 316
m24	0.25	27	4.5	AF	LCb	0-6.5	12	169.7, -17.1	
					MCa	6.5-195	27	111.8, -1.9	
m25	0.19	14	10.3	AF	U	0-9.5	17	169.7, -17.1	
					U	9.5-70	77	352.9, 8.7	
m26	0.17	34	11.4	AF	LCb	0-10.5	20	204.9, 9.2	
m27	0.20	220	9.9	AF	LCb	0-30	54	188.5, -11.8	149, 1483
m28	0.14	84	9.5	AF	LCb	3-17.5	30	165.1, -21.0	134, 1051
m29	0.21	7.3	10.1	AF	LCb	1-16	31	189.8, -3.7	
LCa							20	92.4, -83.3	
MCa							14	109.9, -2.0	
LCb							5	183.9, -9.2	

Note: All samples in table are mutually oriented to within ~5°. For comparison, the mean direction and 95% confidence interval of the three post-accretional overprints are given at the end of the table. The first column gives the sample name; the second column give the mass; the third column gives the mass-normalized NRM moment; the fourth column gives the distance to the fusion crust surface measured from the edge of the sample nearest the fusion crust; the fifth column gives the type of demagnetization applied; the sixth column gives the component name; the seventh column gives the coercivity or temperature range of the component; the eighth column gives the number of AF or thermal steps in each component or the number of samples in a mean direction; the ninth column gives the direction of the component as calculated from PCA or mean direction; the tenth column gives the ARM and IRM paleointensities for samples where both sets of paleointensity experiments were performed.

Table S3: Summary of paleomagnetic results from non-dusty olivine-bearing chondrules

Sample	Mass (mg)	NRM moment (10^{-4} A m^2 kg^{-1})	Component	AF range (mT)	*N*	Dec, Inc (°)	MAD (°)	DANG (°)
C1	0.14	0.37	LC	0-22.5	9	63.6, 28.2	11.5	11.9
			HCa	22.5->290	8	196.5, -21.6		
C2	0.27	0.89	LCa	0-5	3	66.5, -48.8	22.0	17.5
			HCa	5-32.5	8	325.1, 72.2		
C3	0.60	1.2	LC	0-10	5	23.1, 45.9	14.5	11.6
			HCa	10->290	12	233.5, 21.7		
C4a	0.14	0.42	LCa	0-15	7	157.7, -53.3	20.4	4.7
			HCa	15-140	9	274.8, 25.8		
C4b	0.18	0.20	HCa	0-12.5	6	38.1, -12.0	18.8	8.3
C5a	0.22	0.72	LCa	0-10	5	251.4, -53.6	17.2	23.2
			HCa	12.5->290	11	300.8, 25.4		
C5b	0.07	1.5	LC	0-12.5	6	60.0, 0.9		
			HCa	12.5->290	11	237.1, -72.7	8.9	19.2
LCa					20	92.4, -83.3	8.9	
MCa					14	109.9, -2.0	11.7	
LCb					5	183.9, -9.2	19.2	

Note: All samples in table are mutually oriented to within ~5°. All samples were subjected to AF demagnetization. The first column gives the sample name; the second column give the mass; the third column gives the mass-normalized NRM moment; the fourth column gives the component name; the fifth column gives the coercivity range of the component; the sixth column gives the number of AF or thermal steps in each component or the number of samples in a mean direction; the seventh column gives the direction of the component as calculated from PCA or mean direction; the eighth column gives the maximum angular deviation (MAD) of the component or the 95% confidence interval (α_{95}) of the mean direction (see Section 3.3); the ninth column gives the deviation angle (DANG).

Table S4: Summary of dusty olivine-bearing chondrule paleointensities

Sample	Fitted paleointensity (μT)	Anisotropy-corrected paleointensity (μT)	Total sample uncertainty (2σ; μT)	Rotation-corrected paleointensity (μT)	Rotation-corrected total uncertainty (2σ; μT)
DOC1	29	37	22		
DOC2	22	40.	27		
DOC3	17 (N), 31 (S)	17 (N), 32 (S)	13 (N), 21 (S)		
DOC4	15 (N), 18 (S)	13 (N), 10 (S)	8.9 (N), 10. (S)		
DOC5	19	21	11		
Mean	22.1	27		54	21

Note: The first column gives the sample name; the second column gives the raw ARM paleointensity from a comparison NRM and ARM loss in a given coercivity range with the exception of DOC4S, which has an IRM-based paleointensity; the third column gives the paleointensity after correction for anisotropy using measured anisotropies of ARM acquisition; the fourth column gives the uncertainty in the paleointensity accounting for the statistical uncertainty from linear regression and the uncertainty in the ARM calibration factor *f*; the fifth column gives the paleointensity for the ambient field after correction for the rotation of chondrules during cooling; the sixth column gives the uncertainty in the rotation-corrected paleointensity, taking into account the uncertainty in column four and the uncertainty of the rotation correction (see Section 4).

References

1. K. E. Haisch, E. A. Lada, C. J. Lada, *Astrophys. J. Lett.* **553**, L153 (2001).
2. L. Hartmann, N. Calvet, E. Gullbring, P. D'Alessio, *Astrophys. J.* **495**, 385 (1998).
3. M. Wardle, *Astrophys. Space Sci.* **311**, 35 (2007).
4. X.-N. Bai, J. Goodman, *Astrophys. J.* **701**, 737 (2009).
5. N. J. Turner *et al.*, in *Protostars and Planets VI*. (University of Arizona Press, Tucson, AZ, 2014).
6. R. M. Crutcher, *Annu. Rev. Astron. Astrophys.* **50**, 29 (2012).
7. J. N. Cuzzi, R. C. Hogan, K. Shariff, *Astrophys. J.* **687**, 1432 (2008).
8. T. Nakamura *et al.*, *Science* **333**, 1113 (2011).
9. F. H. Shu, H. Shang, T. Lee, *Science* **271**, 1545 (1996).
10. S. J. Desch, H. C. Connolly, *Meteorit. Planet. Sci.* **37**, 183 (2002).
11. S. J. Desch, T. C. Mouschovias, *Astrophys. J.* **550**, 314 (2001).
12. N. Sugiura, D. W. Strangway, *Proc. Lunar Planet. Sci. Conf. 15th*, C729 (1985).
13. R. R. Fu, E. A. Lima, B. P. Weiss, *Earth Planet. Sci. Lett.* **404**, 54 (2014).
14. H. Leroux, G. Libourel, L. Lemelle, F. Guyot, *Meteorit. Planet. Sci.* **38**, 81 (2003).
15. M. Uehara, N. Nakamura, *Earth and Planetary Science Letters* **250**, 292 (2006).
16. S.-C. L. L. Lappe *et al.*, *Geochem. Geophys. Geosyst.* **12**, Q12Z35 (2011).
17. M. Winklhofer, K. Fabian, F. Heider, *J. Geophys. Res.* **102**, 22695 (1997).
18. I. Garrick-Bethell, B. P. Weiss, *Earth Planet. Sci. Lett.* **294**, 1 (2010).
19. R. J. Reisener, J. I. Goldstein, in *Lunar Planet. Sci. Conf. XXX* (Houston, TX, 1999), pp. 1868.
20. D. Stöffler, K. Keil, E. R. D. Scott, *Geochim. Cosmochim. Acta* **55**, 3845 (1991).
21. R. R. Fu *et al.*, *Science* **338**, 238 (2012).
22. J. Gattacceca *et al.*, *Meteorit. Planet. Sci.* **49**, 652 (2014).
23. C. M. O. D. Alexander, D. J. Barber, R. Hutchison, *Geochim. Cosmochim. Acta* **53**, 3045 (1989).
24. G. D. Cody *et al.*, *Earth Planet. Sci. Lett.* **272**, 446 (2008).
25. B. P. Weiss, E. A. Lima, L. E. Fong, F. J. Baudenbacher, *J. Geophys. Res.* **112**, B09105 (2007).
26. E. A. Lima, B. P. Weiss, R. R. Fu, A. C. Bruno, in *AGU Fall Meeting*. (San Francisco, 2013), vol. GP43B-07.
27. G. S. Watson, *Mon. Not. R. Astr. Soc.* **7**, 160 (1956).
28. C. Suavet, J. Gattacceca, P. Rochette, L. Folco, *Geology* **39**, 123 (2011).
29. S.-C. L. L. Lappe, R. J. Harrison, J. M. Feinberg, A. Muxworthy, *Geochem. Geophys. Geosyst.* **14**, 1 (2013).
30. H. Miura, T. Nakamoto, M. Doi, *Icarus* **197**, 269 (2008).
31. E. H. Levy, S. Araki, *Icarus* **81**, 74 (1989).
32. C. P. McNally, A. Hubbard, M.-M. Mac Low, D. S. Ebel, P. D'Alessio, *Astrophys. J.* **767**, L2 (2013).
33. S. J. Bus, R. P. Binzel, *Icarus* **158**, 146 (2002).
34. X.-N. Bai, *Astrophys. J.* **739**, 1 (2011).
35. S. Mostefaoui *et al.*, *Meteorit. Planet. Sci.* **37**, 421 (2002).
36. M. Lanoix, D. W. Strangway, G. W. Pearce, *Geophys. Res. Lett.* **5**, 73 (1978).
37. P. Wasilewski, *Phys. Earth Planet. Inter.* **26**, 134 (1981).

38. B. P. Weiss, J. Gattacceca, S. Stanley, P. Rochette, U. R. Christensen, *Space Sci. Rev.* **152**, 341 (2010).
39. N. Sugiura, M. Lanoix, D. W. Strangway, *Phys. Earth Planet. Inter.* **20**, 342 (1979).
40. J. Gattacceca, P. Rochette, M. Bourot-Denise, *Phys. Earth Planet. Inter.* **140**, 343 (2003).
41. M. Uehara, J. Gattacceca, H. Leroux, D. Jacob, C. J. van der Beek, *Earth Planet. Sci. Lett.* **306**, 241 (2011).
42. A. J. Brearley, A. N. Krot, in *Metasomatism and the Chemical Transformation of Rock,* D. E. Harlov, H. Austrheim, Eds. (Springer-Verlag, Berlin, 2012), pp. 659-789.
43. A. N. Krot *et al.*, *Meteorit. Planet. Sci.* **33**, 623 (1998).
44. A. N. Krot, E. R. D. Scott, M. E. Zolensky, *Meteorit. Planet. Sci.* **32**, 31 (1997).
45. A. N. Krot *et al.*, *Meteorit. Planet. Sci.* **33**, 1065 (1998).
46. B.-G. Choi, K. D. McKeegan, L. A. Leshin, J. T. Wasson, *Earth Planet. Sci. Lett.* **146**, 337 (1997).
47. S. E. Haggerty, B. M. McMahon, *Proc. Lunar Planet. Sci. Conf. 10th*, 851 (1979).
48. T. F. Stepinski, *Icarus* **97**, 130 (1992).
49. H. Nübold, K.-H. Glassmeier, *Icarus* **144**, 149 (2000).
50. H. C. Spruit, in *NATO ASIC Proc. 477: Evolutionary Processes in Binary Stars,* R. A. M. J. Wijers, M. B. Davies, C. A. Tout, Eds. (1996), pp. 249-286.
51. L. Carporzen *et al.*, *Proc. Natl. Acad. Sci. USA* **108**, 6386 (2011).
52. M. Funaki, T. Nagata, K. Momose, *Mem. Natl. Inst. Polar Res. Spec. Issue* **20**, 300 (1981).
53. M. E. Bennett, H. Y. McSween Jr., *Meteorit. Planet. Sci.* **31**, 783 (1996).
54. C. M. Johns-Krull, *Astrophys. J.* **664**, 975 (2007).
55. C. M. Johns-Krull, T. P. Greene, G. W. Doppmann, K. R. Covey, *Astrophys. J.* **700**, 1440 (2009).
56. J.-F. Donati, F. Paletou, J. Bouvier, J. Ferreira, *Nature* **438**, 466 (2005).
57. R. M. Crutcher, T. H. Troland, B. Lazareff, I. Kazes, *Astrophys. J.* **456**, 217 (1996).
58. E. Falgarone, T. H. Troland, R. M. Crutcher, G. Paubert, *Astron. Astrophys.* **487**, 247 (2008).
59. C. Hayashi, *Sup. Prog. Theor. Phys.* **70**, 35 (1981).
60. S. Chandrasekhar, E. Fermi, *Astrophys. J.* **118**, 113 (1953).
61. J. M. Girart, R. Rao, D. P. Marrone, *Science* **313**, 812 (2006).
62. A. M. Hughes, C. L. H. Hull, D. J. Wilner, R. L. Plambeck, *Astrophys. J.* **145**, 1 (2013).
63. R. J. Reisener, J. I. Goldstein, *Meteorit. Planet. Sci.* **35**, A135 (2000).
64. E. Jarosewich, *Meteoritics* **25**, 323 (1990).
65. R. J. Reisener, J. I. Goldstein, *Meteorit. Planet. Sci.* **38**, 1669 (2003).
66. M. Kimura, J. N. Grossman, M. K. Weisberg, *Meteorit. Planet. Sci.* **43**, 1161 (2008).
67. D. J. Dunlop, O. Ozdemir, *Rock Magnetism: Fundamentals and Frontiers*. Cambridge Studies in Magnetism (Cambridge University Press, New York, 1997), pp. 573.
68. E. R. Rambaldi, J. T. Wasson, *Geochim. Cosmochim. Acta* **46**, 929 (1982).
69. L. E. Fong, J. R. Holzer, K. K. McBride, E. A. Lima, F. Baudenbacher, *Rev. Sci. Instrum.* **76**, 053703 (2005).
70. N. S. Church *et al.*, in *AGU Fall Meeting*. (San Francisco, 2012), vol. GP51B-05.
71. E. A. Lima, B. P. Weiss, L. Baratchart, D. Hardin, E. Saff, *J. Geophys. Res.* **118**, 2723 (2013).

72. E. A. Lima, B. P. Weiss, in *AGU Fall Meeting* (San Francisco, 2012), pp. GP21A-1151.
73. L. M. Pham *et al.*, *New J. Phys.* **13**, 045021 (2011).
74. D. Le Sage *et al.*, *Nature* **496**, (2013).
75. J. L. Kirschvink, *Geophys. J. R. Astr. Soc.* **62**, 699 (1980).
76. J. Gattacceca, P. Rochette, *Earth Planet. Sci. Lett.* **227**, 377 (2004).
77. A. Stephenson, D. W. Collinson, *Earth Planet. Sci. Lett.* **23**, 220 (1974).
78. E. K. Shea *et al.*, *Science* **335**, 453 (2012).
79. S. J. Morden, *Meteoritics* **27**, 560 (1992).
80. S. M. Cisowski, D. W. Collinson, S. K. Runcorn, A. Stephenson, M. Fuller, *Proc. Lunar Planet. Sci. Conf. 13th*, A691 (1983).
81. D. S. Lauretta, P. R. Buseck, T. J. Zega, *Geochim. Cosmochim. Acta* **65**, 1337 (2001).
82. G. Pullaiah, G. Irving, K. L. Buchan, D. J. Dunlop, *Earth Planet. Sci. Lett.* **28**, 133 (1975).
83. D. W. Sears, *Modern Geology* **5**, 155 (1975).
84. A. Stephenson, *J. Geophys. Res.* **98**, 373 (1993).
85. B. P. Weiss *et al.*, *Science* **322**, 713 (2008).
86. C. Suavet, B. P. Weiss, T. L. Grove, *Geochem. Geophys. Geosyst.* **15**, (2014).
87. J. Matas, Y. Ricard, L. Lemelle, F. Guyot, *Contrib. Mineral Petrol.* **2000**, 73 (2000).
88. S. J. Morden, D. W. Collinson, *Earth Planet. Sci. Lett.* **109**, 185 (Mar, 1992).
89. S. M. Tikoo *et al.*, *Earth Planet. Sci. Lett.* **337-338**, 93 (2012).
90. L. Tauxe, H. Staudigel, *Geochem. Geophys. Geosyst.* **5**, doi:10.1029/2003GC000635 (2004).
91. T. Nagata, *Proc. Lunar Planet. Sci. Conf. 13th*, A779 (1983).
92. M. Jackson, *Pageoph* **136**, 1 (1991).
93. P. A. Selkin, J. S. Gee, L. Tauxe, W. P. Meurer, A. J. Newell, *Earth Planet. Sci. Lett.* **183**, 403 (2000).
94. A. Stephenson, *Geophys. J. R. Astr. Soc.* **73**, 213 (1983).
95. N. Sugiura, D. W. Strangway, *Earth Planet. Sci. Lett.* **62**, 169 (1983).
96. Y. Usui, J. A. Tarduno, M. Watkeys, A. Hofmann, R. D. Cottrell, *Geochem. Geophys. Geosyst.* **10**, Q09Z07 (2009).
97. E. W. Weisstein, Sphere point picking. In Series MathWorld- A Wolfram Web Resource. http://mathworld.wolfram.com/SpherePointPicking.html.
98. A. Papoulis, *Probability, Random Bariables and Stochastic Processes*. (Mcgraw-Hill College, New York, ed. 3, 2002).
99. A. Tsuchiyama *et al.*, in *Lunar Planet. Sci. Conf. XXXIV*. (Houston, TX, 2003), pp. 1271.
100. D. J. Gendzwill, M. R. Stauffer, *Math. Geol.* **13**, 135 (1981).
101. C. C. Ferguson, *Math. Geol.* **11**, 329 (1979).
102. R. Brown, *http://www.mathworks.com/matlabcentral/fileexchange/15125-fitellipse-m*, (2007).
103. E. W. Weisstein, Circle point picking. In Series Mathworld- A Wolfram Web Resource. http://mathworld.wolfram.com/CirclePointPicking.html.
104. T. J. McCoy, T. L. Dickinson, G. E. Lofgren, *Meteorit. Planet. Sci.* **34**, 735 (1999).
105. W. Feller, *An Introduction to Probability Theory and Its Applications*. (John Wiley & Sons, New York, 1966), vol. II.
106. S. J. Peale, in *Planetary Satellites,* J. A. Burns, Ed. (University of Arizona, Tucson, AZ, 1977).

107. D. Morin, *Introduction to Classical Mechanics: With Problems and Solutions*. (Cambridge University Press, 2008), pp. 734.
108. F. Reif, *Fundamentals of statistical and thermal physics*. E. U. Condon, Ed., McGraw-Hill international editions: Physics series (McGraw-Hill, Singapore, 1985).
109. F. J. Ciesla, D. S. Lauretta, L. L. Hood, *Meteorit. Planet. Sci.* **39**, 531 (2004).
110. R. R. Fu, B. P. Weiss, *J. Geophys. Res.* **117**, E02003 (2012).
111. H. C. Connolly, R. H. Hewins, N. Atre, G. E. Lofgren, *Meteoritics* **29**, 458 (1994).
112. G. J. Herczeg, L. A. Hillenbrand, *Astrophys. J.* **681**, 594 (2008).
113. S. A. Balbus, J. F. Hawley, *Astrophys. J.* **376**, 214 (1991).
114. J. F. Hawley, S. A. Balbus, *Astrophys. J.* **376**, 223 (1991).
115. X.-N. Bai, J. M. Stone, *Astrophys. J.* **769**, 76 (2013).
116. G. Lesur, M. W. Kunz, S. Fromang, *Astron. Astrophys.* **566**, A56 (2014).
117. X.-N. Bai, *Astrophys. J.* **791**, 137 (2014).
118. R. D. Blandford, D. G. Payne, *Mon. Not. R. Astr. Soc.* **199**, 883 (1982).
119. C. F. Gammie, *Astrophys. J.* **457**, 355 (1996).
120. X.-N. Bai, *Astrophys. J.* **772**, 1 (2013).
121. S. J. Desch, *Astrophys. J.* **608**, 509 (2004).
122. R. Salmeron, M. Wardle, *Mon. Not. R. Astr. Soc.* **345**, 992 (2003).
123. M. W. Kunz, *Mon. Not. R. Astr. Soc.* **385**, 1494 (2008).
124. C. Phatak, M. Tanase, A. L. Petford-Long, M. De Graef, *Ultramicroscopy* **109**, 264 (2009).